AFRL-AFOSR-JP-TR-2022-0010

Science-based Automation of Composites Manufacturing

Anoush Poursartip
UNIVERSITY OF BRITISH COLUMBIA, THE
6190 AGRONOMY RD STE 102
VANCOUVER, BC, V6T 1Z3
CAN

12/03/2021
Final Technical Report

Air Force Research Laboratory
Air Force Office of Scientific Research
Asian Office of Aerospace Research and Development
Unit 45002, APO AP 96338-5002

REPORT DOCUMENTATION PAGE	*Form Approved* *OMB No. 0704-0188*

1. REPORT DATE *(DD-MM-YYYY)* 03-12-2021	**2. REPORT TYPE** Final	**3. DATES COVERED** *(From - To)* 01 Jul 2020 - 28 Sep 2021

4. TITLE AND SUBTITLE
Science-based Automation of Composites Manufacturing

5a. CONTRACT NUMBER

5b. GRANT NUMBER
FA2386-20-1-4020

5c. PROGRAM ELEMENT NUMBER

6. AUTHOR(S)
Anoush Poursartip

5d. PROJECT NUMBER

5e. TASK NUMBER

5f. WORK UNIT NUMBER

7. PERFORMING ORGANIZATION NAME(S) AND ADDRESS(ES)
UNIVERSITY OF BRITISH COLUMBIA, THE
6190 AGRONOMY RD STE 102
VANCOUVER, BC V6T 1Z3
CAN

8. PERFORMING ORGANIZATION REPORT NUMBER

9. SPONSORING/MONITORING AGENCY NAME(S) AND ADDRESS(ES)
AOARD
UNIT 45002
APO AP 96338-5002

10. SPONSOR/MONITOR'S ACRONYM(S)
AFRL/AFOSR IOA

11. SPONSOR/MONITOR'S REPORT NUMBER(S)
AFRL-AFOSR-JP-TR-2022-0010

12. DISTRIBUTION/AVAILABILITY STATEMENT
A Distribution Unlimited: PB Public Release

13. SUPPLEMENTARY NOTES

14. ABSTRACT
There is strong need in composites manufacturing to further enhance quality, reliability, and production rates. Here, I4.0 digital technologies are integrated and customized for composites manufacturing. A table-top AFP simulator dispensing a single prepreg tow under controlled conditions has been designed. The system can measure peel resistance of the deposited prepreg in-situ. This allows for independent characterization of layup/peel speed, substrate orientation, and tack time effects. A new smart roller measures pressure at the AFP nip point. Future expansion of the AFP cell, smart roller, and integration of physical and virtual digital twins are discussed.

15. SUBJECT TERMS

16. SECURITY CLASSIFICATION OF:			**17. LIMITATION OF ABSTRACT**	**18. NUMBER OF PAGES**	**19a. NAME OF RESPONSIBLE PERSON**
a. REPORT	**b. ABSTRACT**	**c. THIS PAGE**			JEREMY KNOPP
U	U	U	SAR	72	**19b. TELEPHONE NUMBER** *(Include area code)* 315-227-7006

FA2386-20-1-4020

SCIENCE-BASED AUTOMATION OF COMPOSITES MANUFACTURING

Nima Bakhshi, Oliver Tong, Ziqiang Chen, Dr. Mirza Saquib Sarwar, Dr. John Madden, Dr. Anoush Poursartip

Composites Research Network

University of British Columbia

June 2021

TABLE OF CONTENTS

Section Page

TABLE OF CONTENTS I
LIST OF FIGURES III
LIST OF TABLES IV
ACKNOWLEDGEMENTS V
1.0 EXECUTIVE SUMMARY 1
2.0 INTRODUCTION 2
2.1 Science-Based Automation of Composites Manufacturing 2
2.2 Automated Fiber Placement 3
2.3 Characterization of Prepreg Tack 4
2.3.1. Peel Test 4
2.3.2. Probe Test 6
2.4 Physics-based Modeling of Prepreg Tack 8
2.5 Physics-based Simulation of the AFP Process 10
3.0 METHODS, ASSUMPTIONS, AND PROCEDURES 11
3.1 Sense-Think-Act Framework 12
3.2 AFP Simulator: Physical Digital Twin 14
3.3 AFP Simulator: Virtual Digital Twin 15
4.0 RESULTS AND DISCUSSION 15
4.1 ACT 15
4.1.1. AFP Simulator Dispenser 15
4.1.1.1 Prepreg Deposition 15
4.1.1.2 In-situ Peel Mechanism 16
4.1.1.3 Compaction System 17
4.1.1.4 Heating System 19
4.1.1.5 Material Handling and Delivery System 21
4.1.1.6 Tow Tension Considerations 24
4.1.1.7 Spool Design and Wind/rewind Considerations 26
4.1.2. Design of the Gantry System 29
4.1.2.1 Tool Setup 35
4.1.3. Design of the control and electrical systems 36
4.1.4. Summary 39
4.2 Sense 40
4.2.1. First set of Standard Sensors 40
4.2.2. Smart Roller 41
4.2.2.1 Smart Roller: Introduction and Operating Principles 41
4.2.2.2 Smart Roller: Design 42
4.2.2.3 Roller Mechanical Performance: Background 45
4.2.2.4 Roller Mechanical Performance: Approach 49
4.3 Think 54
4.3.1. High-fidelity Physics-based Models 54

4.3.2. Real-time Virtual Twin 56
4.3.3. Integrated Modeling Approach 56
5.0 CONCLUSIONS 58
6.0 REFERENCES 60
7.0 SYMBOLS, ABBREVIATIONS AND ACRONYMS 63

LIST OF FIGURES

Page

Figure 1. Schematic of the AFP process. 3
Figure 2. Continuous application and peel method of tack characterization. 5
Figure 3. Peel test sample [6]. 5
Figure 4. A typical test result from the peel test. 6
Figure 5. Probe test method of tack characterization. 6
Figure 6. A typical test result from the peel test. 7
Figure 7. Fibril/cavity growth in a pressure sensitive adhesive [14]. 7
Figure 8. Cohesive failure of prepreg tack and fibrillation [10]. 8
Figure 9. Resin bleeds into the gaps between the two adjacent layers [15]. 9
Figure 10. Rate- and temperature-dependent tack model. 9
Figure 11. Simulation of prepreg disposed on a steered trajectory. 10
Figure 12. Sense-think-act framework. 13
Figure 13. Sense-think-act system development. 14
Figure 14. Schematic of prepreg deposition. 16
Figure 15. Schematic of in-situ peel test. 17
Figure 16. Compaction system. 18
Figure 17. Geometry of the heated area. 20
Figure 18. Infrared heating system. 21
Figure 19. Kinematic simulation of material spool motion used for motor sizing. 22
Figure 20. Material handling servo system. 24
Figure 21. Deviation from the ideal spiral geometry in a roll. 25
Figure 22. Sample ultrasound sensor from Montalvo. 26
Figure 23. Formation of transition zone and deviation from ideal geometry in a cylindrical spool. 26
Figure 24. Material spool design. 27
Figure 25. Approximate methods for estimating rolled length. 29
Figure 26. Naming convention and service life of the linear axis [23]. 31
Figure 27. Proposed planar gantry layout. 32
Figure 28. Gantry's maximal effort motion profiles. 33
Figure 29. Bridge axis as a double-fixed beam. 34
Figure 30. CAD design of the gantry. 35
Figure 31. Front view schematic of the tool and gantry setup. 36
Figure 32. Architecture of the automation platform. 37
Figure 33. Control system modules and their functions. 38
Figure 34. Control system assembly. 39
Figure 35. AFP Simulator. 39
Figure 36. Force sensors. 40
Figure 37. A typical sensor cell and its deformation under pressure and shear loading. 42
Figure 38. Roller interior and exterior. 42
Figure 39. Schematics of the sensor. 43
Figure 40. Completed assembly of the sensor. 44
Figure 41. Completed roller assembly. 44
Figure 42. Smart roller contact region and measured output. 45
Figure 43. Segmented roller with linear degree of freedom [27]. 46
Figure 44. Segmented roller with rotation degree of freedom [28]. 47
Figure 45. Geometrical relationship between trajectory and roller [32]. 48

Figure 46. Baseline compaction roller. 49
Figure 47. Compaction pressure distributions (MPa) in the baseline compaction roller at three different levels of process compaction force. 50
Figure 48. Preliminary characterization of the roller tire material under compression.. 51
Figure 49. Geometry of the smart roller.. 52
Figure 50. Compaction pressure (CPRESS) distributions of the rollers subjected to 240 N. 53
Figure 51. High-fidelity deposition model.. 54
Figure 52. Cohesion sub-model of deposition. 54
Figure 53. Decohesion model. 55
Figure 54. Process-microstructure-property relationship.. 57
Figure 55. Integrated Analysis Framework.. 57
Figure 56. Process-microstructure-property relationship in the integrated framework. 58
Figure 57. First set of AFP experiments. 59

LIST OF TABLES

Page
Table 1. Parameters related to sizing of the heating system. 21
Table 2. Strength limits of the slides and bearings [23]. 30

ACKNOWLEDGEMENTS

Financial and intellectual support from the project sponsor, US Air Force Research Laboratory and Dr. John Russell, is gratefully acknowledged. Authors would like to thank support from the industrial and academic members of the Composites Research Network (CRN). Constructive discussions with Dr. Alireza Forghani and Malcolm Lane (Convergent Manufacturing Technologies), Dr. Casey Keulen (UBC CRN), Scott Nesbitt (UBC CRN), Dr. Christoph Sielmann (UBC), Dr. Homayoun Najjaran (UBCO), Dr. Michael Kupke and Florian Krebs (DLR Augsburg), and Dr. Ali Yousefpour (National Research Council Canada) are gratefully apreciated.

1.0 EXECUTIVE SUMMARY

Advanced polymer-matrix composite materials are revolutionizing commercial and military aviation. However, to increase our use of composites, we need to develop methods to reliably and efficiently make bigger and more complex structures at higher production rates. To date, automation has been an obvious route to more effective manufacturing but has not been as successful as desired. Our working hypothesis is that modern digital technologies, typically captured under the heading of Industry 4.0, are not being effectively and appropriately applied to composites manufacturing. At the most fundamental level, the peculiarities and specific needs of composites manufacturing are not being recognized and addressed.

The current project investigates the application of industry 4.0 approaches to composites manufacturing. We study the best strategies to get maximum value of an integrated approach to digitalization, thus overcoming the weaknesses of any individual digital technology. The anticipated short-term outcome is an understanding and strategy on how to best use Industry 4.0 technologies to increase productivity in an AFP cell, and the long-term outcome is a blueprint for general strategies for how to best deploy Industry 4.0 technologies in the whole factory, thus enabling the successful digital industrialization of composites manufacturing.

With this project, a small but representative automated fiber placement simulator cell, with complete with a range of sensors is under development. A smart, instrumented roller is being developed to measure compaction pressure at the nip point of the process. The AFP simulator cell is supported by physics-based simulations, data sciences (artificial intelligence/machine learning), and uncertainty quantification methods.

The project was started in July 2020, and this report covers the first year of activity. Design details of the different sub-systems involved in the AFP cell are discussed in the present report. A dispenser has been designed to dispense a single prepreg tow under controlled temperature, pressure, and speed. The AFP cell uses a table-top gantry system to produce the required layup motion. In addition to controlling the layup temperature, independent temperature control is provided for the entire tool. An industrial grade control system is used to control all the systems of the AFP cell and gather all sensor data, centrally. Furthermore, development of the first operational version of the smart roller is reported and plans for further development of the roller to measure other relevant properties and enhance its characteristics are discussed.

Development of the Physical Digital Twin (i.e. the AFP simulator cell) is near completion and the final steps of system assembly are being carried out. A framework for developing the Virtual Digital Twin and integrating the results with the Physical Digital Twin has been developed. State-of-the-art of physics-based simulations relevant to AFP have been identified and the modeling approach is discussed. Once both digital twins are setup, the systems will be run over a wide range of process parameters to generate data. Influence of different process parameters on tack and process quality outcomes will be investigated. Moreover, the physical and virtual digital twins will be integrated to pursue the project objectives.

2.0 INTRODUCTION

2.1 Science-Based Automation of Composites Manufacturing

The use of composites in aerospace has grown dramatically since the commercialization of carbon fiber in the 1960s [1]. This growth has been fueled by many new commercial and military programs, all with bigger and/or more complex composite structures. At the same time, there are expectations of better performance, lower cost, and faster rates of development; there is an availability of ever more material choices; and there is the retirement of experienced people at the same time as the need for more people. Increasingly it is clear that a major impediment to even greater use of composites is our inability to routinely engage in low risk, agile, low cost manufacturing without sacrificing performance [2]. Although automation has been a major enabler for decades now [3], the success has been lower than expected. For example, we are still unable to make complex parts using AFP in a fast and robust manner [4], and any change in material, geometry or process condition requires extensive testing.

All of this is happening in the much broader context of the digitalization of manufacturing, with Industry 4.0 now a commonly used term to describe a digital world where designs are optimized for manufacturing, smart automated factories are built up to perfectly execute on the manufacturing, and every part built is fully monitored and documented per specification and at the expected cost. But the question must be: how easy will it be to bring Industry 4.0 to composites manufacturing when we have had so many issues to date?

To understand why composites manufacturing has not benefitted from automation we must acknowledge that aerospace composites manufacturing is fundamentally different from other manufacturing sectors. For example, a single widebody commercial airplane, although it has a value comparable to 200,000 smartphones, has by design very different (and optimized) structural components throughout. Strategies developed for other products, materials and processes do not translate directly. We need to explicitly address those issues that are specific to composites in a framework which benefits from all the general developments in materials and manufacturing [5].

Current research and technology development is primarily focused on improving the individual enabling digital technologies of automation, sensing, physics-based simulation and the data sciences/uncertainty quantification. The significance and innovation of the present work is to integrate these capabilities and customize them for composites manufacturing. In this manner, we can compensate for weaknesses in each individual digital technology and create significant value from the integration.

The project objective is to evaluate the best strategies to effectively and efficiently industrialize composites manufacturing using digital Industry 4.0 approaches. A small but representative automated fiber placement (AFP) simulator cell, equipped with a range of sensors, and supported by physics-based simulation, data science (artificial intelligence/ machine learning) and uncertainty quantification approaches is being built. This demonstration cell will be used to investigate why size/complexity scaling and production scaling are so difficult in composites manufacturing. We will test the hypothesis that digital benefit is only truly achieved when the five enabling digital technologies are appropriately combined to benefit from their individual strengths and compensate for their individual weaknesses. The short-term objective is to identify how to best use Industry 4.0 technologies to increase productivity in an AFP cell and the long-term objective is to develop general strategies for how to best deploy Industry 4.0 technologies in a whole factory. To do this, we will generalize our findings into a proposed blueprint to scale up our findings to industrial size problems, and to other automated manufacturing processes.

2.2 Automated Fiber Placement

Automated Fiber Placement is one of the automated technologies that is increasingly used in the aerospace industry to manufacture high quality, large-scale and complex parts. This technology offers higher productivity, quality consistency and reliability compared to traditional manufacturing methods. AFP consists of a dispenser (also called AFP head) responsible for transferring and dispensing prepreg tape at the nip point of the process. Moreover, a gantry system or a robotic arm is used to move the dispenser over the designed layup trajectories.

Narrow prepreg tows or prepreg slit tapes of width 3.2, 6.4 or 12.7 mm (1/8, 1/4 or 1/2 in) are usually used in AFP processing. Individual tows are pulled from material storage spools. The backing paper protecting one side of the prepreg is separated and the prepreg is fed through a tow delivery system to the AFP head. Several tows (up to 32 tows in parallel) are collimated on the compaction roller to form a wider band, called a course, and are placed onto the tool surface by application of heat and pressure (Figure 1).

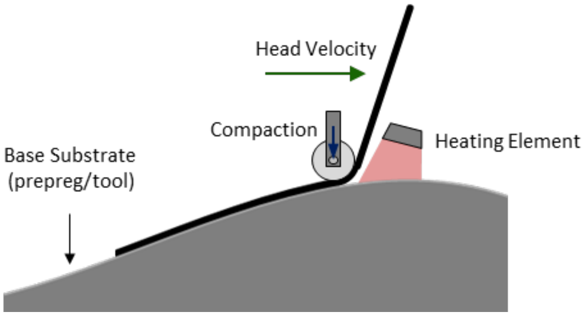

Figure 1. Schematic of the AFP process.

Several factors contribute to or resist formation of process-induced defects in AFP. When the layup trajectory deviates from tool geodesic between the starting and end point points of the trajectory, the prepreg tow will be inclined to shift toward the local geodesic (since the prescribed path is not the path of minimum potential energy). Various conditions, including tow steering and tool curvatures, can result in residual stresses that will further increase the tow's propensity to deviate from the prescribed layup path to release the stored energy. During deposition, the prepreg tow interacts with the compaction roller in a complex manner that can initiate some of the defects that are observed in the process.

On the other hand, the main mechanism that resists formation of defects in the process is tack, or adhesiveness, of prepreg. When prepregs are disposed under high pressures and elevated temperatures, prepreg resin behaves in a compliant and tacky manner and will be able to form a cohesive bond with the previous substrate. Traction forces resulting from tack help the prepreg to remain on the prescribed layup path. Therefore, a comprehensive understanding of tack behavior under AFP conditions is crucial for a successful layup. Most common methods to characterize prepreg tack are presented in the next section.

2.3 Characterization of Prepreg Tack

2.3.1. Peel Test

The standard method of characterizing prepreg tack is the continuous application and peel procedure described in ASTM D8336 -21 [6]. The apparatus consists of two pairs of stiff rollers. The left pair (Figure 2, a) supports the specimen. The top right roller (peel roller), guides the prepreg sample to go through a 90° peel from the substrate while the bottom right roller (compaction roller) is spring loaded and provides the compaction force required for application of the prepreg to the substrate. If prepreg/prepreg tack is being characterized, another prepreg layer is bounded to the substrate, otherwise for prepreg/tool tack characterization prepreg comes into direct contact with the substrate. The free end of the prepreg is fixed to the testing machine's head and the prepreg layer is fed through the test fixture continuously. The compaction roller presses the prepreg against the substrate at a controlled force and rate. Simultaneously, prepreg is peeled off, at the same time it is coming into contact with the substrate. Therefore, compaction or development of tack cohesion, and peel-off or decohesion happen in a single stage, necessarily at the same rate. Measured tack is specified in terms of a peel force at a given specimen width.

The sample consists of two phases (Figure 3). The prepreg face is protected with backing paper in phase I, while it comes into direct contact with the substrate in phase II. Only the second phase includes the prepreg tack response, as cohesion is prevented in phase I. Phase I characterizes dissipative effects in the system such as friction, prepreg dynamic stiffness and other inefficiencies. The difference between the average loads recorded in phases I and II, is the average tack force (Figure 4). The test can be performed inside an environmental chamber to control temperature and humidity during the tests. Further information on development of the continuous application and peel test method, analysis approach, characterization of effects of process and environmental parameters (i.e. substrate, speed, compaction force, temperature and humidity) on tack and its trends, as well as viscoelastic time-temperature equivalence and development of tack master curves can be found in [7],[8],[9],[10],[11].

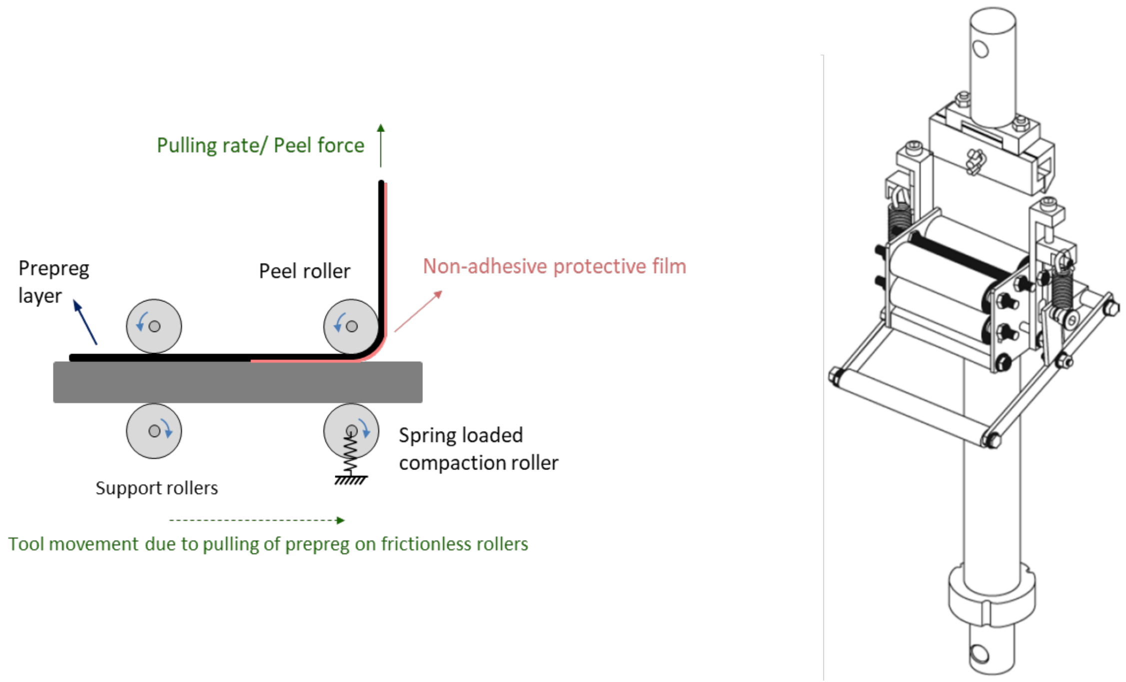

(a) Schematic **(a) Apparatus** [6]

Figure 2. Continuous application and peel method of tack characterization.

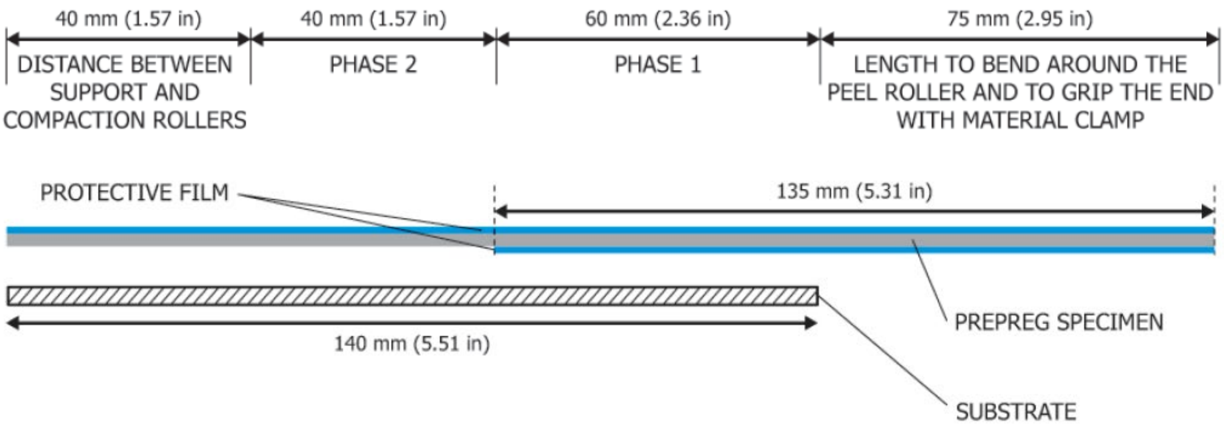

Figure 3. Peel test sample [6].

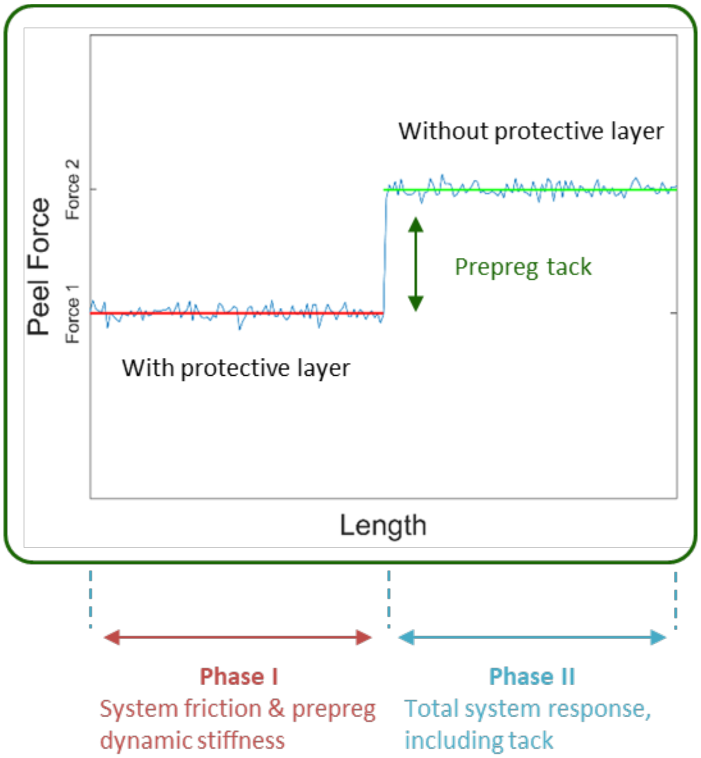

Figure 4. A typical test result from the peel test.

2.3.2. Probe Test

In the probe test method, a probe with a circular cross-section is brought into contact with a prepreg sample, until a prescribed amount of compaction force is reached. It remains in contact with the sample for duration of dwell time, then it starts to retract from the sample. As the probe is pulled away, displacements and resistance forces are measured. The method can be performed in a rheometer to have accurate control over temperature and humidity of the tests. Influence of various material, process and environmental parameters on prepreg tack were studied in [12],[13] using the probe test method.

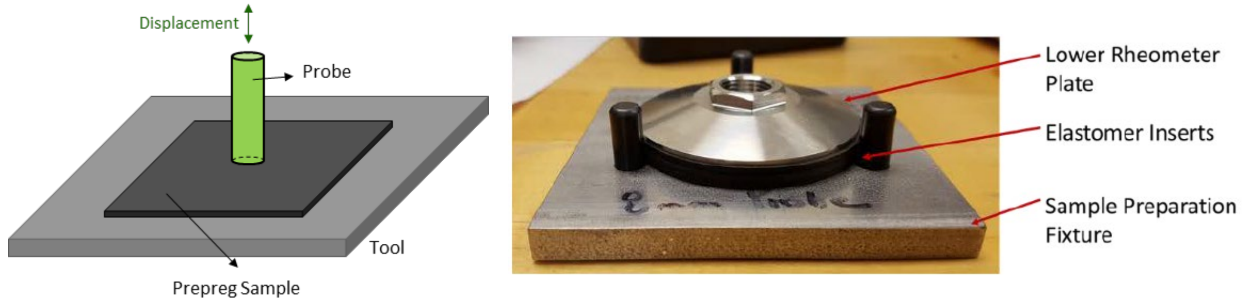

(a) Schematic

(b) Probe test fixture designed to be used on a rheometer [13]

Figure 5. Probe test method of tack characterization.

The probe test method is able characterize the shape of the traction-separation curve of tack response. Figure 6, shows a typical result of this experiment. The tack force first rapidly increases during the initial retraction, reaches a peak, and then rapidly drops in value. The post-peak decline can be attributed to formation of fibril, i.e., continuous resin filaments between the probe and prepreg surface. Once the fibrils are formed, they will elongate significantly, until they break. Figure 7 shows fibril/cavity growth during tack decohesion for a pressure sensitive adhesive film [14] at the probe cross-section. In Figure 7, (a) is the point of peak traction, (b) is at the end of the first rapid drop, and (c) is at the end of fibril elongation. It is important to note the same fibrillation phenomenon was also observed by Crossley et al. [10] during cohesive failure of prepreg tack in the peel tests (Figure 8).

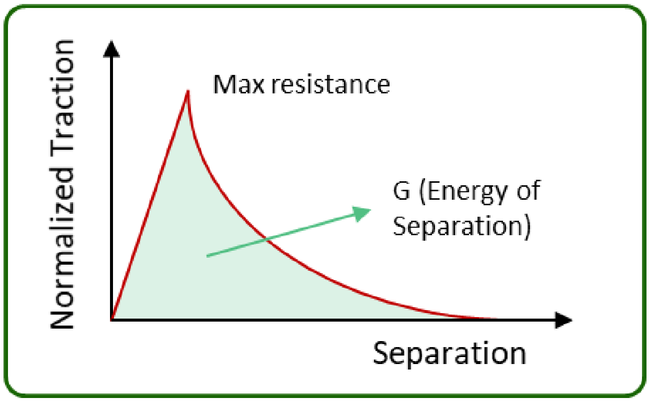

Figure 6. A typical test result from the peel test.

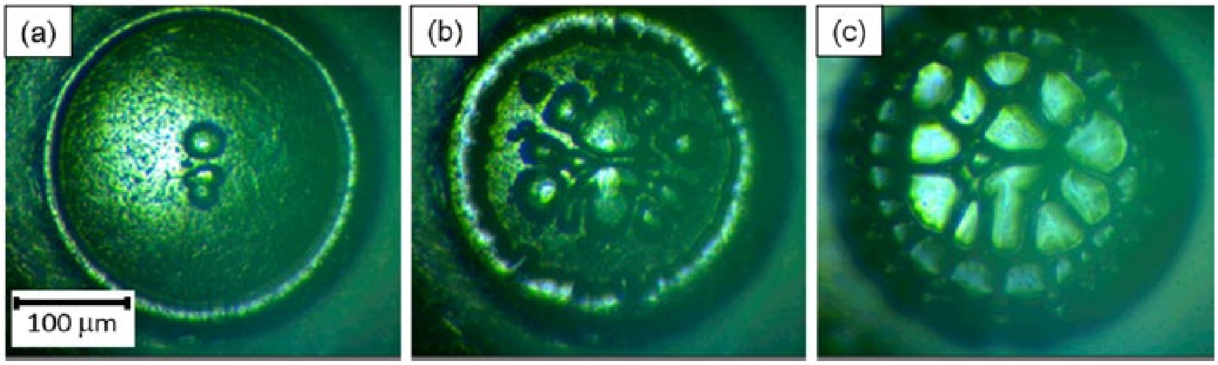

Figure 7. Fibril/cavity growth in a pressure sensitive adhesive [14].

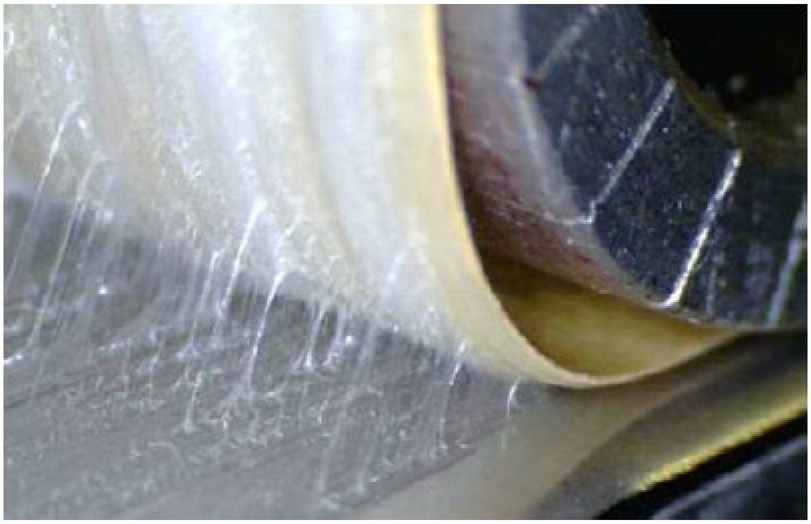

Figure 8. Cohesive failure of prepreg tack and fibrillation [10].

2.4 Physics-based Modeling of Prepreg Tack

A state-of-the-art physics-based model for tack was developed under NASA Advanced Composites Project (ACP) [15],[16]. The developed tack model consists of two stages, cohesion and decohesion. During the cohesion stage, prepreg surfaces are brought into contact. Resin bleeds into the gaps between the two adjacent layers by squeeze flow of the resin and shear flow of the fibers. The resin bleed into the inter-laminar micro-voids is characterized by the resin flow index:

$$FI = \int \frac{P(t)}{\mu(t)} dt \tag{1}$$

Where P is pressure and μ is dynamic viscosity of the resin. Uncured resin viscosity is a function of temperature. Therefore, for a given prepreg, pressure history, temperature history and head speed affect the flow index.

Resin bleed (Figure 9) is the primary mechanism that allows for an intimate contact to form between the two adjacent prepreg layers. The level of intimate contact achieved in the process is quantified using a non-dimensional parameter called Degree of Intimate Contact (DoIC). The value of DoIC ranges from 0 to 1; 0 corresponding to no cohesion and 1 corresponding to complete cohesion. Degree of Intimate Contact is an intermediate state variable introduced in the model to quantify the state of cohesion at the end of this process. Flow index, process dwell time, aging, moisture content and surface roughness are among the parameters that can influence the degree of intimate contact.

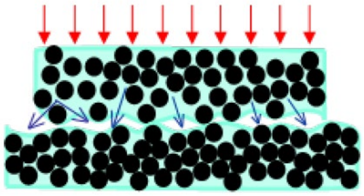

Figure 9. Resin bleeds into the gaps between the two adjacent layers [15].

The decohesion stage of the tack model takes the backbone viscoelastic response of the resin and reduces it for the true contact conditions achieved in the process, by utilizing the concept of degree of intimate contact. This model predicts the peak value of the traction-separation response curve as well as the Energy of Separation (EoS).

A standard viscoelastic model is used to represent the rate and temperature dependent viscoelastic tack response prior to peak (Figure 10). The stress response of the normal tractions (mode I) of this model is:

$$\sigma = C(DoIC)\left[\sigma_r + \sigma_{g-r}\right] \tag{2}$$

The parameter $C(DoIC)$ introduces dependency on the degree of intimate contact to the pre-peak response [16]. Moreover:

$$\begin{gathered} \sigma_r = E_r\left(\frac{\delta}{h}\right) \\ \sigma_{g-r} = E_{g-r}\left(\frac{\delta}{h}\right) - \frac{\sigma_{g-r}}{\tau}\Delta t \end{gathered} \tag{3}$$

where E_r and E_g are the rubbery and glassy moduli of the resin, $\boldsymbol{\delta}$ is the opening, h is the thickness of the inter-ply interface and $\boldsymbol{\tau}$ is the time scale associated with stress relaxation. Equations 2 and 3 described the normal tack response. If E_r and E_{g-r} are replaced by G_r and G_{g-r} (rubbery and shear glass moduli of the resin) the extension of the model to modes II and III of shear is derived.

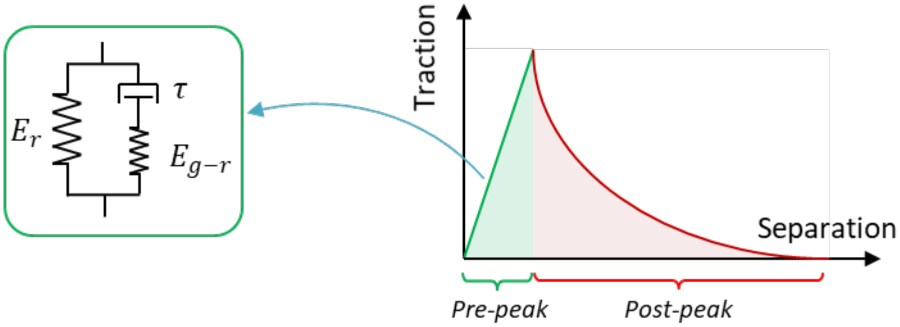

Figure 10. Rate- and temperature-dependent tack model.

A mixed mode opening based criterion is used to establish onset of damage initiation.

$$\left(\frac{\delta_n}{\delta_{ni}}\right)^2 + \left(\frac{\delta_{t2}}{\delta_{t2i}}\right)^2 + \left(\frac{\delta_{t3}}{\delta_{t3}}\right)^2 = 1 \tag{4}$$

where n denotes normal or mode I interactions, t2 and t3 denote shear mode II and mode III interactions. A continuum damage progression approach is used to quantify the post-peak response of the model. A mixed-mode reduction parameter, R is defined such that $\sigma_{post-peak} = R\sigma_{peak}$. The exponential decay function describing R is defined as:

$$R = \exp\left(-\left(\left(\frac{\delta_n}{\delta_{ni}}\right)^2 + \left(\frac{\delta_{t2}}{\delta_{t2i}}\right)^2 + \left(\frac{\delta_{t3}}{\delta_{t3}}\right)^2\right)^{\gamma}\right) \tag{5}$$

2.5 Physics-based Simulation of the AFP Process

The state-of-the-art physics-based model for AFP processing was developed under the NASA Advanced Composites Project (ACP) as a part of COMPRO/Abaqus package [17],[18]. This model simulates material behavior during and after the deposition process. Residual stresses and their effect on layup quality outcomes and defects can be predicted for prepreg tows disposed on complex geometries and steered/straight trajectories. Figure 11 shows simulation results for a single prepreg tow disposed on a trajectory steered at a constant radius.

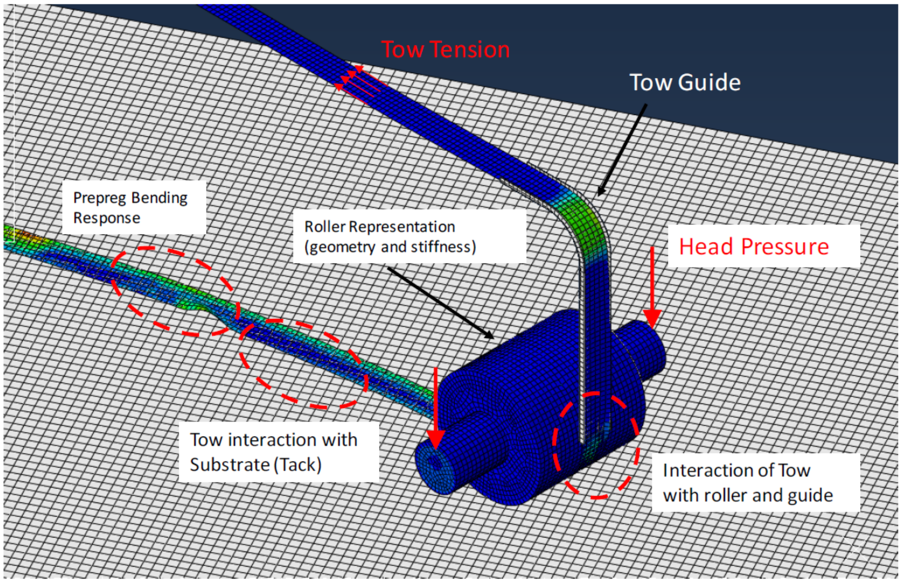

Figure 11. Simulation of prepreg disposed on a steered trajectory.

Within this model, the prepreg tows, compaction roller, tow guides and the substrate are represented. Cohesive interactions between prepreg tows and substrate are captured in the model and prepreg tows are placed on the substrate by imposing displacement boundary conditions on the tows. Finally, the Abaqus/Explicit finite element solver was used to solve the models.

It is known the classic plate theory cannot be used to predict the out-of-plane behavior of uncured prepregs from in-plane material properties. Therefore, prepreg materials are simulated by superimposing membrane and shell formulations to achieve de-coupled axial and flexural behaviors that can be defined independently. The physics-based prepreg tack model developed previously is introduced to the AFP simulation model via 'Cohesive Zone Modelling' between contacting surfaces.

3.0 METHODS, ASSUMPTIONS, AND PROCEDURES

We believe that the correct approach to the problems discussed in section 2.1 is to merge what have previously been two relatively independent thrusts: classic Industry 4.0 approaches which are control and measurement driven, and factory/equipment centric [19]; and integrated computational materials and manufacturing science approaches which are science driven and materials/product centric [20]. Out of this fusion come five enabling technologies, each individually valuable and powerful, but with the real breakthrough coming when they are integrated into a coherent and cohesive strategy. The five enabling technologies are described below, and their individual strengths and weaknesses detailed:

Automation holds great promise to provide repeatable, controlled, and fast material deposition. However, it requires the cost-effective design, building, and operation of equipment that can perform the required material deposition to an appropriate level of precision and quality. The problem is that often we do not know how to specify what is good enough but not excessive. For example, in an AFP machine, what is an acceptable metric for lap and gaps? Too big of a gap, and the performance is not achieved, yet the tighter the requirement, the slower and/or more expensive the solution. What is the ideal speed, pressure, and temperature to run the AFP head? Currently nearly all of control and optimization is done by trial and error [4].

Sensing: There is considerable interest and activity in developing new sensor technologies and systems, and there is no doubt that significant advances are being made. However, we are hamstrung that often we cannot easily measure what we need to measure (what is the temperature exactly at the nip point of the AFP roller?) nor can we be smart in using the sensors in direct feedback loops. We do not know how tightly we should control most parameters: what should the temperature and/or pressure at the nip point be? To what tolerance?

Data Sciences: The ability to manage, aggregate, and reduce large amounts of data using artificial intelligence, including machine learning and other methods has revolutionized sensor technologies such as image recognition, as well as creating algorithms that can predict outcomes in very complex problems. Unfortunately, much of current data science approaches require enormous amounts of training data that are not available in composites manufacturing.

Uncertainty Quantification: The field of statistics and uncertainty quantification has exploded in recent years, especially with the wholesale embrace of Bayesian statistics across many disciplines. Although many would lump UQ within the data sciences, UQ is an enabling technology in its own right as it allows for the fusion of sensor data with physics-based simulation

Physics-based simulation has proven to be of great value in describing and quantifying many manufacturing issues, including thermal, quality and residual stress outcomes. Physics-based simulation has the strong benefit of proposing causality of events rather than correlation, but suffers from the fact that it is currently difficult to do much more than predict the mean response of a manufacturing process, and the models are good but not perfect.

The value of an integrated approach: We propose that an integrated development and deployment of the five enabling technologies will provide enormous value and be the disruptive enabler for composites manufacturing. The ground truth of physics-based simulation can be converted into fast and usable theory-guided machine learning algorithms, which can then be tuned for inverse optimization applications. Uncertainty quantification can be used to combine relatively sparse data from sensors with the theory-guided machine learning algorithms to provide meaningful analysis and feedback for the automated system. This can be done not just in one factory cell, but across factory cells: material out-time can be factored into AFP deposition parameters, and defects can be allowed at the AFP cell if it is known that they can be eliminated during cure. Conversely, what appears to be acceptable features in the AFP cell can be identified as the trigger for defect generation during cure.

3.1 Sense-Think-Act Framework

The sense-think-act framework has been the leading paradigm in the field of robotics for decades [21]. Originally developed in the fields of robotics, control and automation, this framework states that a robot needs to sense its location with respect to its surrounding, think through potential solutions for performing the desired activity, plan ahead, and finally, execute the planned motion independently using available actuators.

In the automated fiber placement industry, ample work has been performed on 'path planning' which focuses on determining proper actuation of the robotic arm to produce the intended layup path on complex tool geometries.

This work aims to apply the sense-think-act framework with a material processing centered perspective (Figure 12). We are fundamentally interested in understanding what process or material parameters are important to measure during the AFP processing for effective prediction and control of quality outcomes (sense). Then, the data measured from the process is analyzed in the physics-based framework for understanding of the system (think), in order to finally determine, how can we establish the AFP process window scientifically in an effective and efficient manner (act).

A standard set of sensors is employed to measure process parameters. Additionally, a smart roller is under development to measure process parameters at the nip point of the AFP process, in an in-situ manner. The physics-based framework used for analysis of the AFP system includes physics-based modeling and simulation of various physical phenomena involved in the AFP process. With regards to process control, it is of interest to identify the most informational parameters, i.e., process or material parameters that can describe the state of the AFP process most effectively. Moreover, it is important to be able to establish the processing window scientifically using process parameters measured during the manufacturing process.

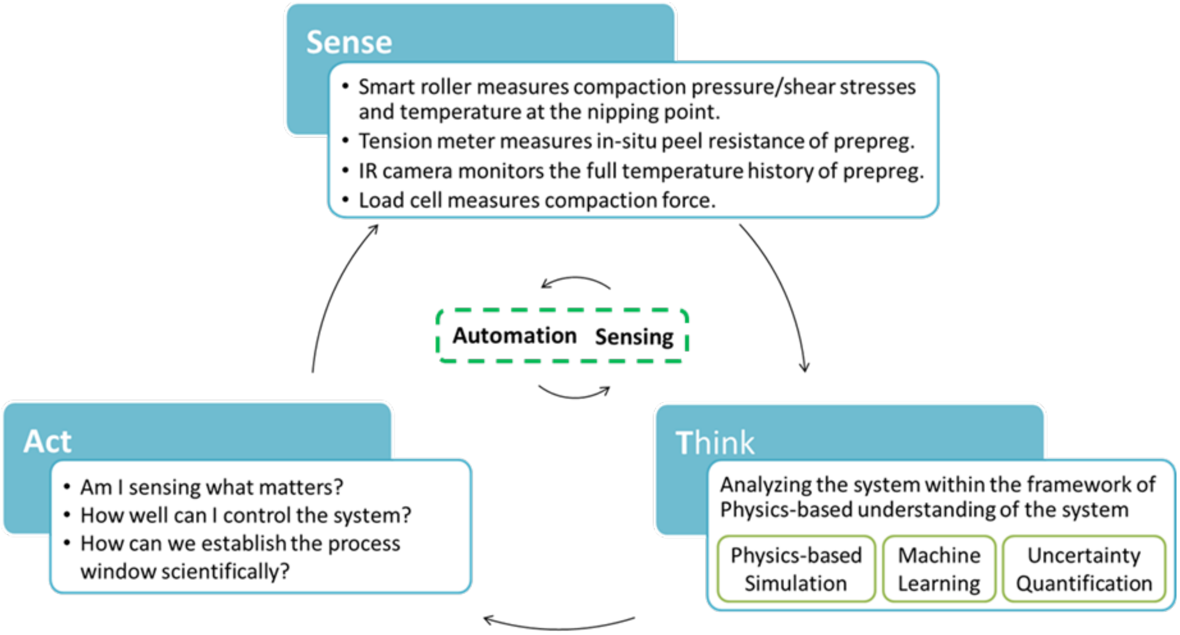

Figure 12. Sense-think-act framework.

When considering the process through the lens of the sense-think-act framework, it is often observed that one of these elements have progressed significantly while the other ones are lagging. For example (Figure 13, a), very advanced sensor technology may be used to monitor the process. But what if the available physics-based frameworks are unable to offer accurate interpretations or insights into the process and relevance of the measured parameter to material processing? This necessarily leads to inability to act or control the process efficiently, resulting in untapped capacity in the system. We believe that the most effective and efficient approach to automation is a balanced integration of sensing, thinking, and acting within an automated manufacturing system (Figure 13, b). This concept is applicable to all of composites manufacturing, especially more modern technologies with high potential for automation, including but not limited to, Automated Fiber Placement, forming and Additive Manufacturing.

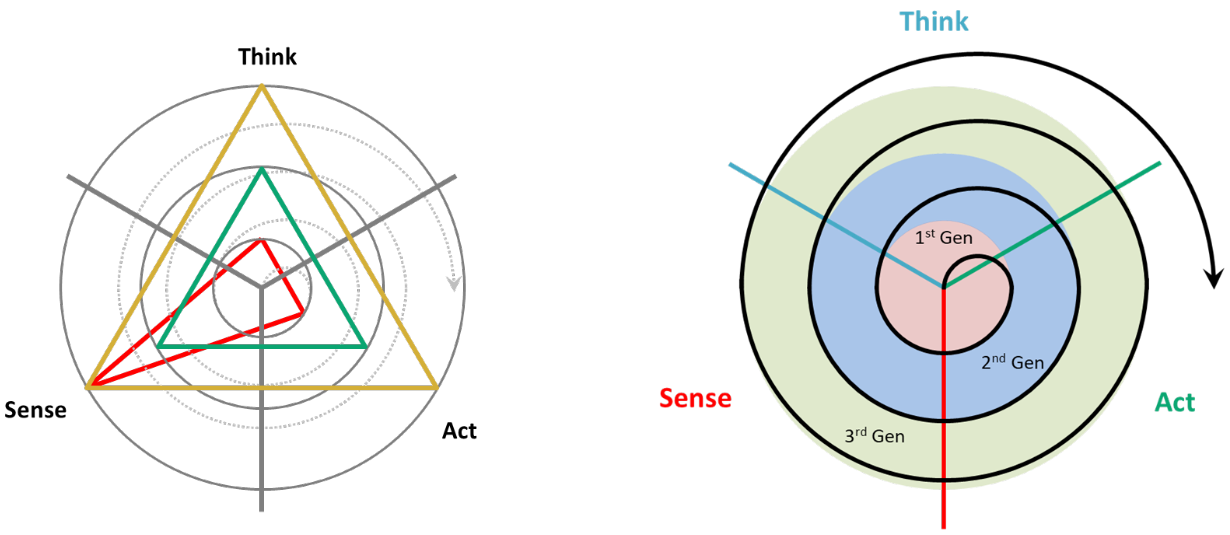

(a) Unbalanced vs balanced progression of sense-think-act

(b) Balanced integration concept

Figure 13. Sense-think-act system development.

3.2 AFP Simulator: Physical Digital Twin

In order to investigate the application of industry 4.0 approaches to composites manufacturing, a small but representative AFP simulator (Physical Digital Twin) is being built. Industrial scale AFP systems are typically too complex and large to allow for the flexibility required to perform an in-depth analysis of the process. It is too difficult to alter them as needed, install custom sensing technology, and large clearance distances from the robot/equipment are required to avoid collision. The table-top simulator designed and built in this work performs the primary functions of a fiber placement system using a single tow, hence, it is studied as a representative model system. Section 4.1 discusses design of the various parts of the AFP simulator.

The two most common methods of measuring prepreg tack, probe tack test and peel test, were reviewed in 2.3. Each one of these methods have their own specific strengths and weaknesses. The probe test is very easy to perform. More importantly, it is able to characterize the shape of tack traction-separation response curve during the initial elastic response, as well as the irreversible damage propagation phase. However, the test geometry is quite different from tow deposition or defect growth in the AFP process. Furthermore, the timescales in the probe test are typically larger than the timescales during the AFP processing, and they are limited by the reactiveness of the universal testing machine used. Typically, it may take more than 0.5 – 1 seconds for the probe to come into contact with the prepreg, reach the prescribed compaction force, and start to retract. In comparison, during the AFP process the time under pressure for a given length of prepreg tow (i.e. dwell time) can be in the order of milliseconds. For example, if prepreg tows are disposed at the rate of 1 m/s using the industrial roller in Section 4.2.2.5, the dwell time is ~10 ms. This suggests the best bond qualities reached during the AFP process is inferior to the worst bond qualities achievable by probe test.

The standard peel test method uses a geometry that is much more similar to AFP deposition.

Therefore, the measured quantity is more representative of the tack demonstrated in the process. While the peel test is an excellent approach for characterization of prepreg tack, it is aimed here to further improve it. The AFP simulator is designed to be able to perform in-situ peel tests. Essentially, prepreg tows are first dispensed in a manner similar to AFP deposition, then, the dispenser peels the prepreg tow off the tool surface (see 4.1.1.1 and 4.1.1.2 for more details). This method offers a few advantages. Time required for sample preparation is much reduced, as samples are made by the table-top AFP system. The setup performs deposition and peel in two separate steps; therefore, effects of peel rate and deposition rate can be studied and characterized independently. Moreover, by controlling the time elapsed between deposition and peel, potential effects of stress relaxation during AFP processing can be characterized. It is commonly observed during production that defects may grow hours after layup was completed. A second generation of the AFP simulator will be equipped with the ability to steer prepreg tows. The steering capability will allow for characterization of potential effects of curvatures and residual stresses on demonstrated tack levels.

3.3 AFP Simulator: Virtual Digital Twin

As will be discussed in Section 4.4 an integrated analysis framework has been developed for studying the present system. Physics-based models, ML and UQ approaches will be used to develop a virtual twin of the AFP simulator. Process conditions used in the physical twin will be simulated in the virtual twin. Physical data will be integrated into the virtual data obtained from physics-based models to further analyze the process.

4.0 RESULTS AND DISCUSSION

Results and discussions related to project’s progress are presented in this section. Following the sense-think-act framework, the content of this section is presented in three parts. Starting with development of the Physical Digital Twin, Section 4.1 presents efforts spent on design and building of various sub-systems involved in an AFP simulator (act). Section 4.2 presents sensor technologies used in the simulator to monitor relevant process parameters, including the smart roller (sense). Section 4.3 presents efforts devoted to developing the integrated analysis framework for this project (think).

4.1 Act

4.1.1. AFP Simulator Dispenser

4.1.1.1 Prepreg Deposition

The dispenser of the table-top AFP is responsible for storage and delivery of a single tow of prepreg, dispensing prepreg tows under controlled compaction force and temperature and performing in-situ peel tests. The mechanism of performing the in-situ peel test is described in 4.1.4, while the remaining systems used for providing the basic functionalities are disclosed in the following sections. Figure 1 presents a 2D schematic of prepreg deposition with the simulator’s dispenser. Deposition temperature is controlled using power controlled infrared emitters, and a pneumatic cylinder provides the required compaction force. The material spool is fully motorized, and its rotational speed is controlled using a Variable Frequency Drive. Tow tension during both deposition and peel is measured using a tension transducer.

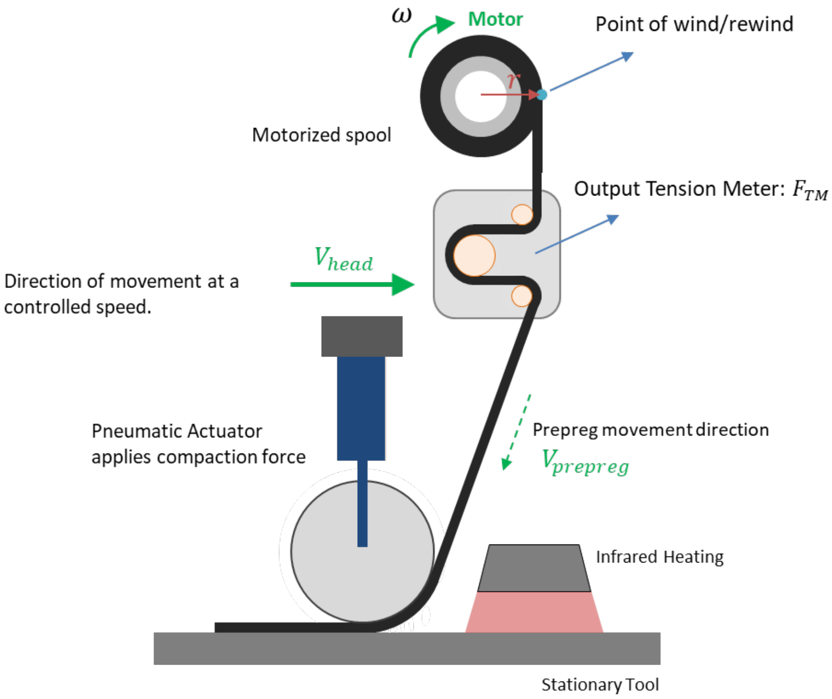

Figure 14. Schematic of prepreg deposition.

4.1.1.2 In-situ Peel Mechanism

One of the key features of the developed AFP simulator is the additional capability to perform in-situ peel tests under real AFP conditions. The necessity to develop this feature was discussed in section 3.2. The overall procedure for performing the in-situ peel test is schematically described in Figure 15. After the prepreg tow is disposed on the tool surface, the AFP head starts to move in the reverse direction (opposite of the deposition direction). Simultaneously, the motorized material spool will start to rewind the prepreg tow, in a synchronous manner. Under controlled conditions, where the linear speed of the prepreg tow is equal to the linear speed of the dispenser head, the amount of tension measured in the prepreg tow is equal to peel resistance, i.e. tack.

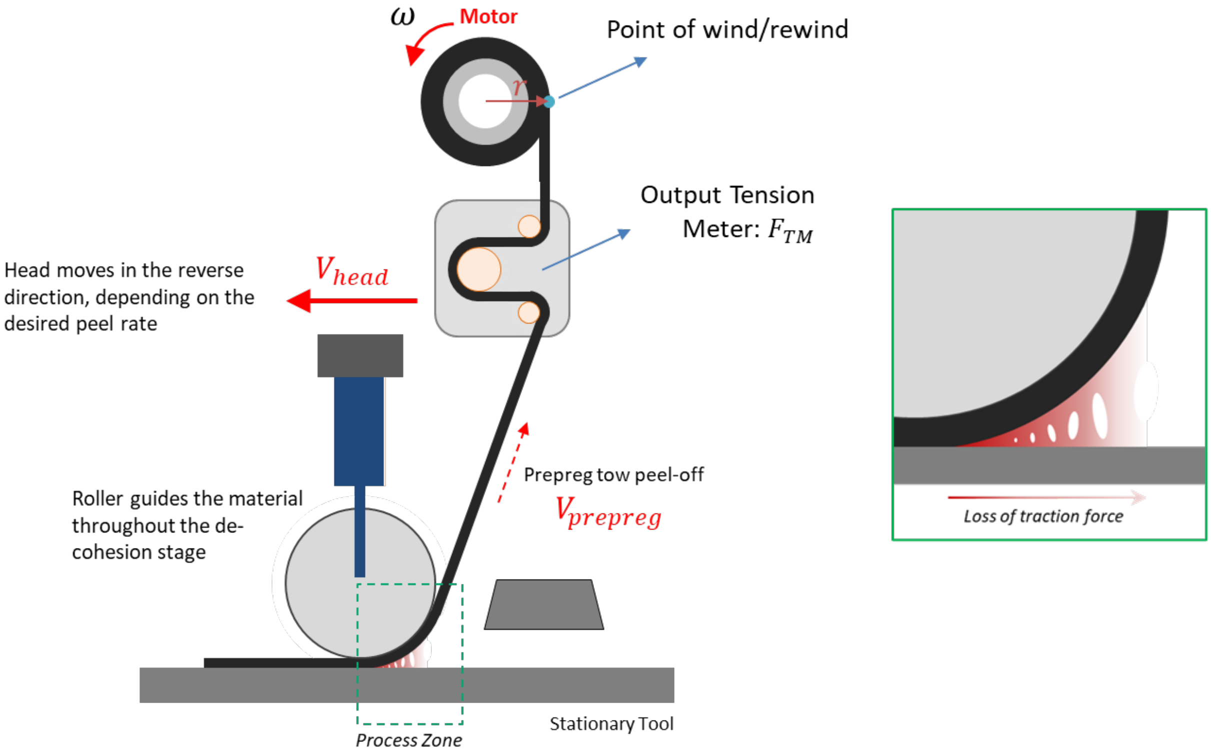

(a) Schematic of in-situ peel test

(b) Tack decohesion during peel

Figure 15. Schematic of in-situ peel test.

For the in-situ peel test to perform as intended, it is crucial for the linear speed ($V_{prepreg}$) of the prepreg to be equal the speed of the head (V_{head}). The prepreg tow is essentially anchored down by tackiness of the large piece of prepreg that is already adhered to the tool surface, as well as the additional resistance of the roller. Therefore, if the linear speed of prepreg is larger than that of the AFP head, the spool will start to extend the prepreg tow, resulting in measured tow tension (F_{TM}) that is larger than peel resistance.

Linear speed of prepreg tow is determined by the rotational speed of the material spool and the instantaneous radius of the material spool, as prepreg is rewound ($V_{prepreg} = r\omega$). Sections 4.1.1.6 and 4.1.1.7 will take an in-depth look at controlling the speed for the in-situ peel tests and controlling tow tension during deposition.

4.1.1.3 Compaction System

Typically, pressurized fluids are used as a part of a compaction mechanism to produce the compaction force required to dispose prepreg tows. Here, a pneumatic cylinder is chosen to provide the compaction force. A tension/compression sensor (section 4.2.1) is installed between the cylinder and the compaction roller to continuously monitor and control the output of the cylinder.

A compressor first compresses the air, then the compressed air is filtered and dehumidified, and fed into a proportional pressure regulator. The proportional pressure regulator is able to set the output pressure of the compressed air automatically, using a signal that is controlled by the central IPC (Industrial PC/controller).

A double-acting compact pneumatic cylinder is used to produce the compaction force. Using two rods and a piston, this cylinder resists against rotation and ensures perpendicular orientation of the compaction roller to the layup trajectory. Moreover, the additional rods increase the cylinder's capacity to support moment arms perpendicular to the piston axis. The cylinder is able to operate with compressed air pressures between 1 and 10 bar and its theoretical force at 6 bar is 295 N.

A 5/3, four-way electrical directional control valve is used to change the direction of the cylinder motion. The valve is in exhaust mode when not excited to ensure safety. Components of the compaction system are shown in Figure 16.

(a) Air compressor **(a) Proportional pressure regulator**

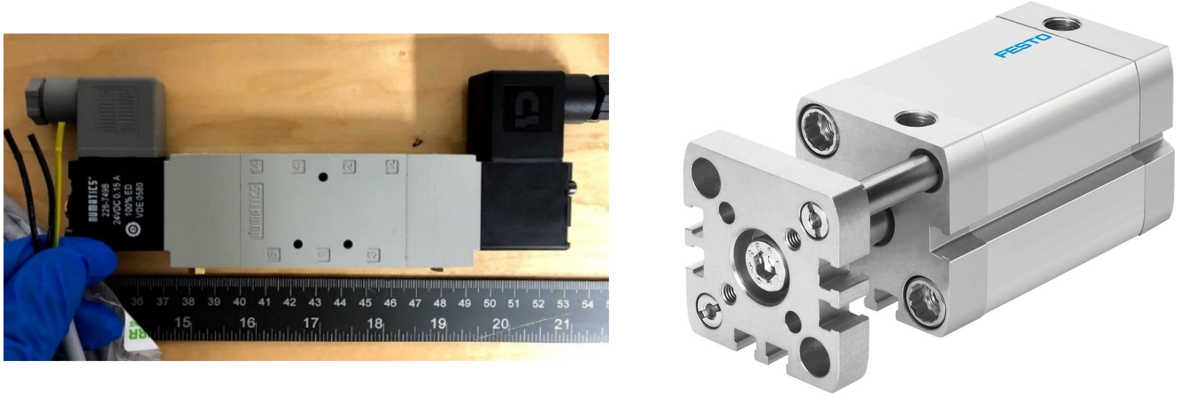

(c) Electronic directional valve **Pneumatic cylinder**

Figure 16. Compaction system.

4.1.1.4 Heating System

Different technologies exist for producing the required temperature during layup including hot gas torch, infrared lamp, laser, and Xenon flash lamp (Humm3 system). An important upper bound exists for temperature in AFP processing of thermoset prepreg tows at about 60 ºC to avoid triggering initiation of the resin curing reaction. Moreover, most studies have reported a peak tack response in the 35-45 ºC range with tack decreasing in temperatures above or below this target.

Laser and Xenon flash lamp systems are able to provide enormous bursts of energy that can result in layup temperatures exceeding 400 ºC, making them more suitable for processing of thermoplastics. Infrared lamps, on the other hand, offer a good versatility, low cost, relatively easy implementation, and few safety concerns, and as the result they have been widely adopted for AFP processing of thermoset tows. This technology was chosen to produce the heat required.

A technical paper by Calawa and Nancarrow [22] from Electroimpact provides an approximation method of sizing infrared heaters for the AFP process. First, the total energy required to raise the temperature of 1 cm^2 of the material is estimated (Equation 6).

$$Q_{IR} = mc\Delta T \tag{6}$$

where Q is the total energy, m is mass, c is specific heat and ΔT is the temperature difference. Each infrared emitter has a specific heated height (h_{heated}) based on its design. The heated height is the total length over which infrared rays are emitted and absorbed by the other medium. Total exposure time ($t_{IR\ exp}$) during which surface is under infrared radiation can be estimated using the speed of AFP head, and the heated height provided by the infrared emitters.

$$t_{IR\ exp} = h_{heated}/V_{head} \tag{7}$$

Kirchhoff's law of thermal radiation states that at each specific wavelength a part of the total radiated energy is absorbed, a part of it is reflected, and the remaining part is transmitted through the body. The average absorption, α_{IR}, (i.e. the percentage of absorption of incident energy) of a prepreg surface can be introduced to the heat calculations as an efficiency factor. Assuming perfect radiation and no losses for this estimation, Equations 6 and 7 are combined to calculate the total power required.

$$P_{IR} = \frac{c\ h_{heated}\ w_{heated}}{\alpha_{IR}\ t_{IR\ exp}} = \frac{c\ V_{head}\ w_{heated}}{\alpha_{IR}} \tag{8}$$

where w_{heated} is the heated width, i.e. width of the infrared lamp (naming convection used is consistent with roller orientation, see Figure 17). Irradiance is defined as the radiant flux of power received by a surface per unit area. Mean surface irradiance (E_{mean}) is a good proxy for appropriate sizing of IR lamps which can be compared to the power density provided by the lamp.

$$E_{mean} = \frac{c}{\alpha_{IR}\, t_{IR\,exp}} = \frac{c\, V_{head}\, w_{heated}}{\alpha_{IR}\, h_{heated}} \tag{9}$$

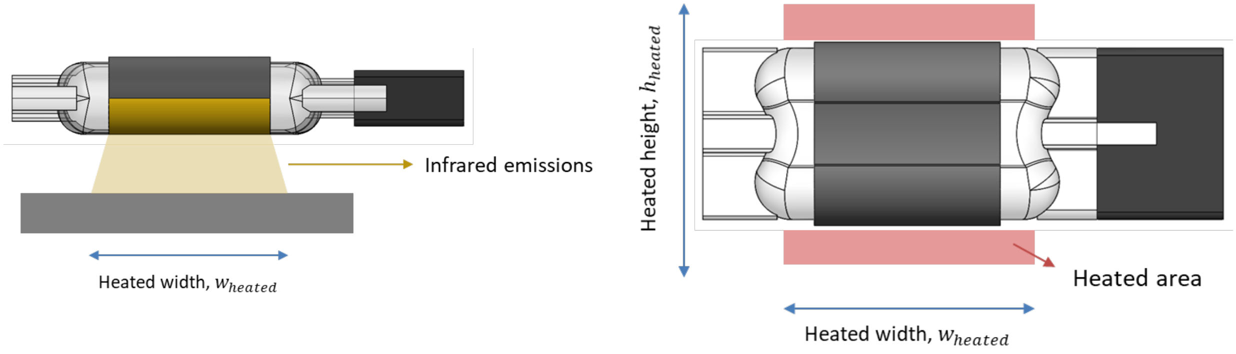

(a) Front view **(b) Top view**

Figure 17. Geometry of the heated area.

For the AFP simulator, two Heraeus twin-tube spotty emitters are used in parallel. Each emitter is rated at 450 watts and 115 V AC. The heated width and height of the emitter are 25 and 23 mm, respectively. Each emitter is manufactured with quartz reflective coating nano reflectors, that eliminate any need for providing more reflective surfaces around the emitter.

Process and material parameters influencing the heat radiation problem are listed in Table 1. The target temperature is assumed to be 45 ºC and a conservative estimation of 0.3 is used for the material's absorption coefficient. The prepreg exposure time to infrared is 33 Milliseconds for the parameters used and a mean surface irradiance of 60.7 (W/cm^2) is found to be required. The spotty emitter chosen for this application can deliver a power density of 78.3 (W/cm^2), meaning 78% of its rated power will be in use under maximal loading conditions.

While form factor and the power density provided by this type of spotty emitter is favorable, it is not designed to be used at high power percentages continuously. Therefore, two emitters will be used side by side, in a parallel configuration. This method increases the exposure time by doubling the heated height, which results in a 50% reduction of the power requirement on each emitter. The reduced power demand helps in increasing lifetime of the emitters. Moreover, it increases system capacity to achieve higher temperatures with higher total power and shorter exposure times, which may be required at higher speeds. The final configuration of the heating system is shown in Figure 1.

Phase-fired control (PFC) is the preferred method of controlling the output power of these emitters. This method, also known as phase angle control, is a method for limiting power in AC systems. A Silicon Controlled Rectifier (SCR) device has been purchased to perform power control using the PFC method. An analog control signal generated by a Beckhoff output module sets the output power of the SCR which is then delivered to the infrared lamps connected in a parallel configuration.

The calculations reviewed here provide a good basis for sizing the heating system. However, as will be discussed in section 4.3, more detailed simulations of the infrared emissions and radiation heat transfer will be required for an accurate physics-based representation and simulation of the existing system.

Table 1. Parameters related to sizing of the heating system.

Parameter	Value
Room temperature (^{o}C)	22
Target temperature (^{o}C)	45
Areal density (g/cm^2)	0.02
Specific heat ($J/g°C$)	1.3
Assumed surface area (cm^2)	1
Average absorption	0.3
Heated height of each emitter (mm)	23
Heated width of each emitter (mm)	25
AFP head speed (m/s)	0.7

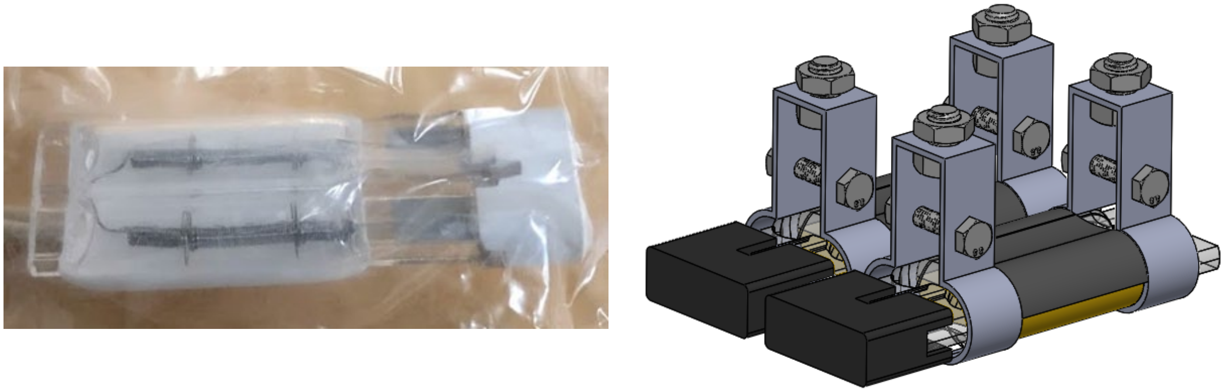
(a) Infrared lamp **(b) CAD assembly of the heating system**

Figure 18. Infrared heating system.

4.1.1.5 Material Handling and Delivery System

Prepreg sheets will be cut into narrow 1/4- to 1/2-inch-wide continuous tapes and will be wound around the material spool manually. Material spool is connected to a Beckhoff servo motor for independent speed control and it is installed on top of the dispenser.

The servo motor is sized using Beckhoff TwinCAT motion designer software. Figure 19 shows the results of kinematic simulations performed. Maximal kinematic conditions the motor may experience were considered for these simulations. Maximum travel of the Gantry's linear axis is 600 (mm). It is assumed that the motion profile consists of three sections, each of which last for 200 (mm) – known as the third rule. It is assumed that 2 (m) of prepreg is already wound around the spool in the beginning of the experiments. In the first 200 (mm), material spool starts to unwind the prepreg tow and accelerate its speed until it reaches the linear payout speed of 1.2 (m/s). Then, it continues tow payout at this rate for another 200 (mm), and finally, starts to decelerate until it reaches the end of travel. Subsequently, the exact same motion profile is repeated but in the opposite direction and material is rewound around the spool. During this stage, a 10 (N) pulling force is applied to the prepreg tow, to simulate peel resistance that should be overcome by motor torque. There may be some off time between the end of the deposition and beginning of the peel test, however, it is neglected in this simulation to estimate maximum demand on the system.

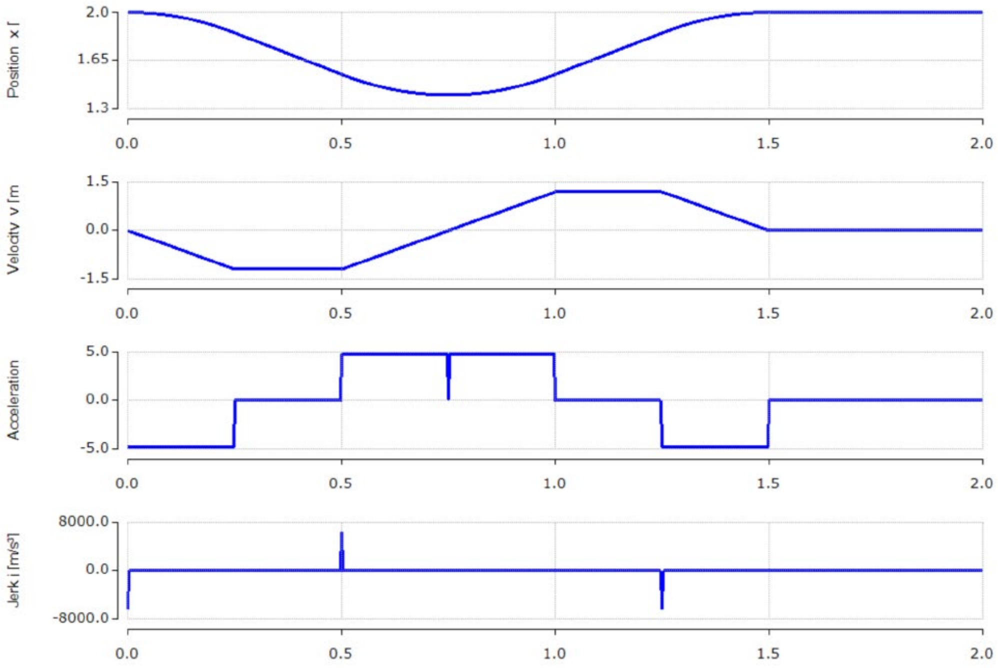

Figure 19. Kinematic simulation of material spool motion used for motor sizing.

Similar to many motor sizing applications, the primary limiting factor is the inertia mismatch between available motor choices and load. In the present application, size and weight are major considerations. A direct drive approach using a gearbox is chosen to assist the motor. When the initial inertia mismatch is high (180 in this application) and a high level of synchronization between different servos is expected, high rigidity of the direct drive will be advantageous compared to other mechanisms such as a timing belt and pulley system. A gearbox with gear ratio of 5 has been chosen. This gearbox reduces the inertia ratio by a factor of 25 and will allow the smallest and lightest servo motor offered by Beckhoff to be used in this application. Using this gearbox helps in reducing the overall cost, weight, and size of the system.

Beckhoff AM8111 servo motor and AG2250-+WPLE40-M01-5 gearbox were chosen for material handling. Figure 20 shows a picture of these devices as well as their simulated performance windows. It is observed that maximum performance requirements of the system are well within the acceptable S1 characteristics curve and nominal limits.

The prepreg tows are protected on one side by backing paper. The backing paper is needed to be removed immediately after the prepreg is unwound from the main spool. A small stepper motor (AS1020-0120 from Beckhoff) equipped with an encoder is used for this application. The motor is connected to a small spool which rotates synchronous to the main material handling motor and winds the backing paper as prepreg is released for deposition.

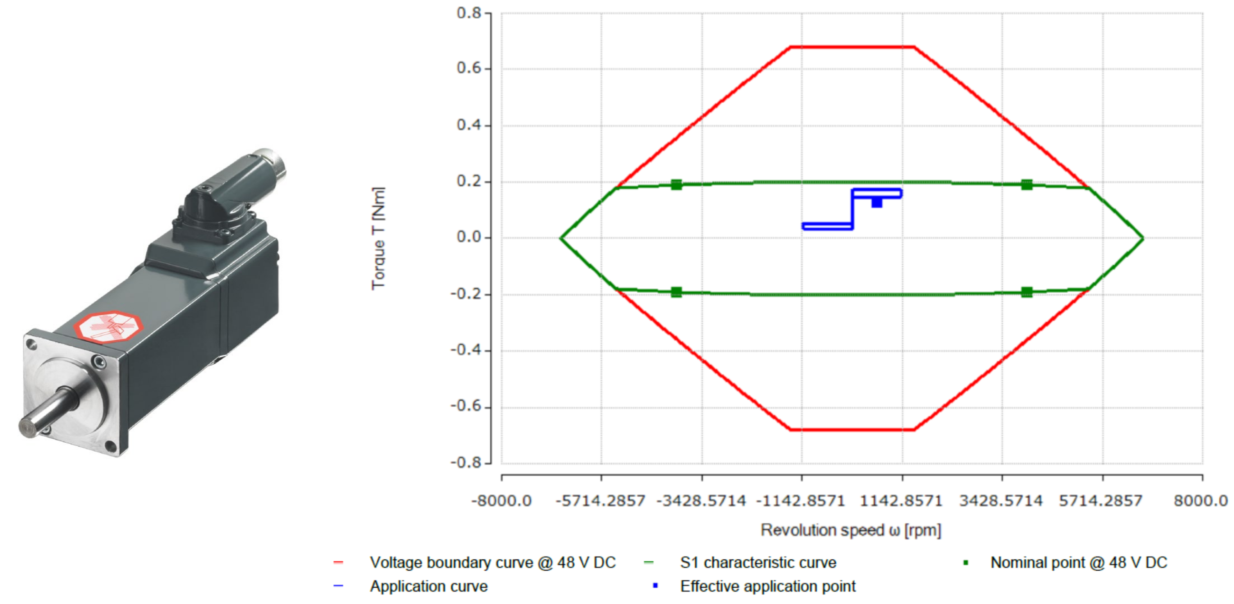

(a) Material handling servo motor

(b) Servo motor performance

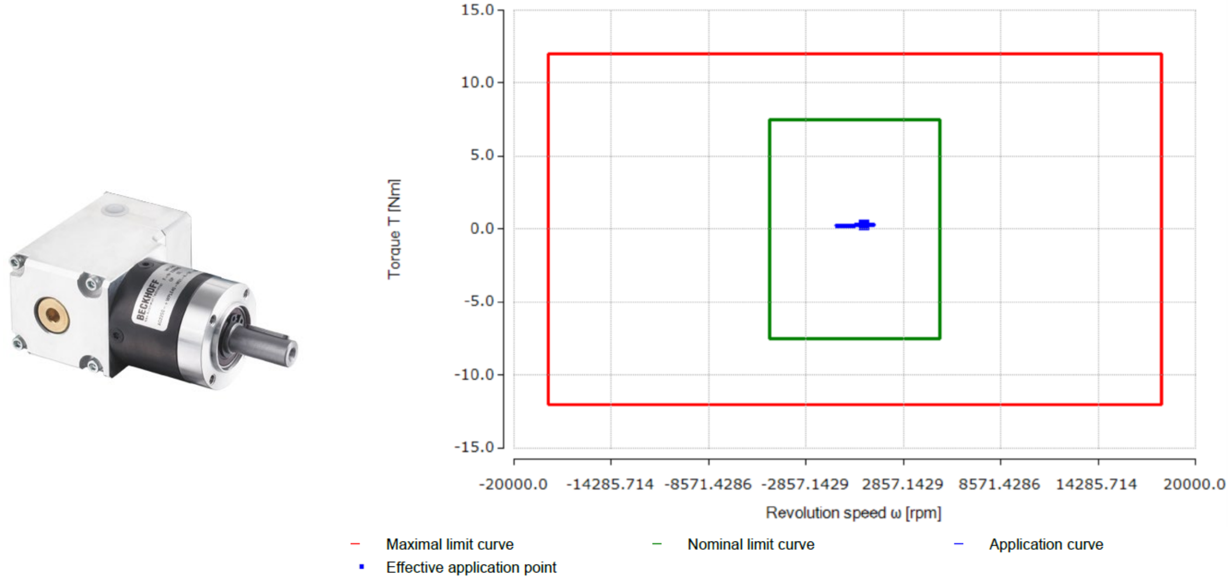

(c) Material handling gearbox

(d) Gearbox performance

Figure 20. Material handling servo system.

4.1.1.6 Tow Tension Considerations

The amount of tension force stored in the prepreg tow is referred to as tow tension. Within this AFP simulator, tow tension is continuously measured using a tension transducer device. During deposition, prepreg tow is anchored onto the tool surface by a combination roller's compaction force and tack, while dispenser moves in the direction of a prescribed trajectory. The rate at which prepreg is released into the process is controlled independently. By adjusting the rate of tow payout tow tension can be controlled.

On the other hand, linear rate of tow rewind should be tightly controlled to measure peel resistance during the in-situ peel test. If prepreg tow is rewound faster than the speed of movement of the dispenser, ($V_{prepreg} > V_{head}$ in Figure 15) the material spool will start to pull and extend the prepreg tow excessively. The resulting strain will create additional tow tension which is detrimental to the peel test. It is when the linear speed of prepreg is equal to the linear speed of the dispenser head, that the amount of tension measured in the prepreg tow is equal to peel resistance, i.e. tack.

This analysis highlights the importance of controlling the linear speed of prepreg both during prepreg deposition and for performing accurate in-situ peel tests. Linear speed of prepreg is dependent on the instantaneous roll radius, and rotational speed of the spool ($V = r\omega$). Instantaneous roll radius changes both during deposition (decreases) and peel (increases). While the instantaneous roll radius changes, the rotational speed of the spool should be controlled appropriately to control the linear speed of the material. There are two issues that need to be addressed.

First issue is the roll shape and its influence on speed. Typically, material spools are of cylindrical shape. When material thickness is not negligible, the shape of the rolled material deviates from the ideal spiral geometry. This might not be an issue when a thin material (such as a paper towel) is rolled around a spool for a large number of turns. In fact, the roll shape will likely converge to the ideal spiral quickly. However, when the material thickness is considerable (Figure 21) and the number of turns on the spool are limited, this issue becomes more pronounced and needs to be accounted for. Second, reliable methods are needed for finding the value of instantaneous radius, which is discussed separately, in Section 4.1.1.7 Wind/rewind Considerations.

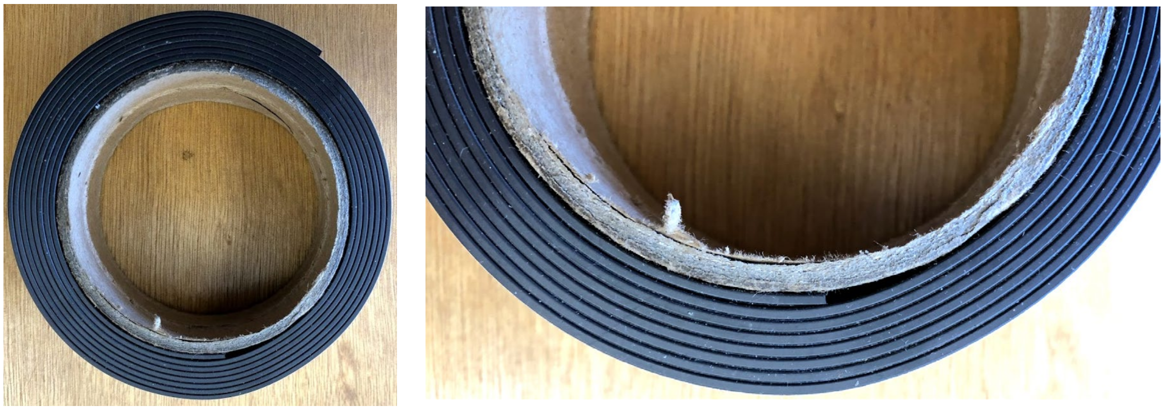

Figure 21. Deviation from the ideal spiral geometry in a roll.

4.1.1.7 Spool Design and Wind/rewind Considerations

Previous discussions established that the primary consideration for the material handling system is management of the effective spool surface radius which changes as the material is wound or unwound. First, a theoretical framework is presented that will be used to calculate the roll radius in real time. Second, ultrasound sensors (Figure 22) for distance measurement can be used to measure spool radius in an in-situ manner. Additionally, image analysis-based linear speed measurements can be used to verify the accuracy of speed control post experiments.

Figure 22. Sample ultrasound sensor from Montalvo.

First, a modified spool design is presented here. The first problem discussed in the Section 4.1.1.6 is summarized in Figure 23. If a cylindrical spool is used for prepreg storage, the finite thickness of prepreg does not allow the spiral geometry to form, and a transition zone will be present for the first several turns of material. Therefore, the AFP simulator's material spool will be manufactured using three-dimensional printing technology, which is highly flexible. The high flexibility of the manufacturing technique is taken advantage of, to produce a spool geometry that is easier to study and use.

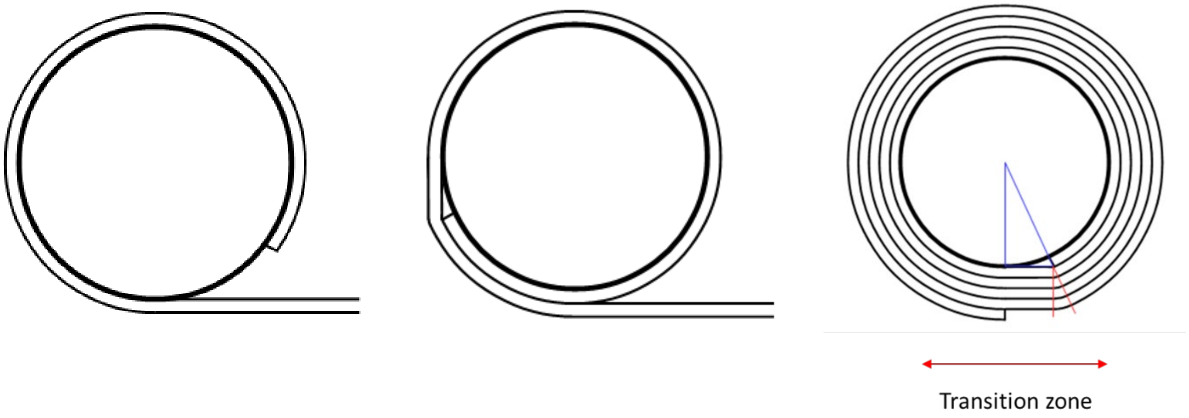

Figure 23. Formation of transition zone and deviation from ideal geometry in a cylindrical spool.

Spool geometry is designed such that its outer radius, follows a spiral shape. The radius starts with the initial value of r_0 (at $\theta = 0\ rad$), then it continues to increase linearly until it reaches the value of $r_0 + h$ after a full turn (at $\theta = 2\pi$). Here, prepreg thickness is denoted by h. Using the spiral roller design, a smooth transition from one layer to the next is ensured. Moreover, prepreg will continuously follow a spiral pattern as it winds or unwinds around the spool. Figure 24 shows the spiral design of the spool. In this figure, prepreg thickness is scaled for better demonstration of the concept. The new design also provides a controlled and clearly identified starting point for the prepreg tow. The spiral equation defining the spool geometry in polar coordinates (r, θ) is presented in Equation 10.

$$r(\theta, t) = r_0 + \frac{\theta(t)}{2\pi} h \tag{10}$$

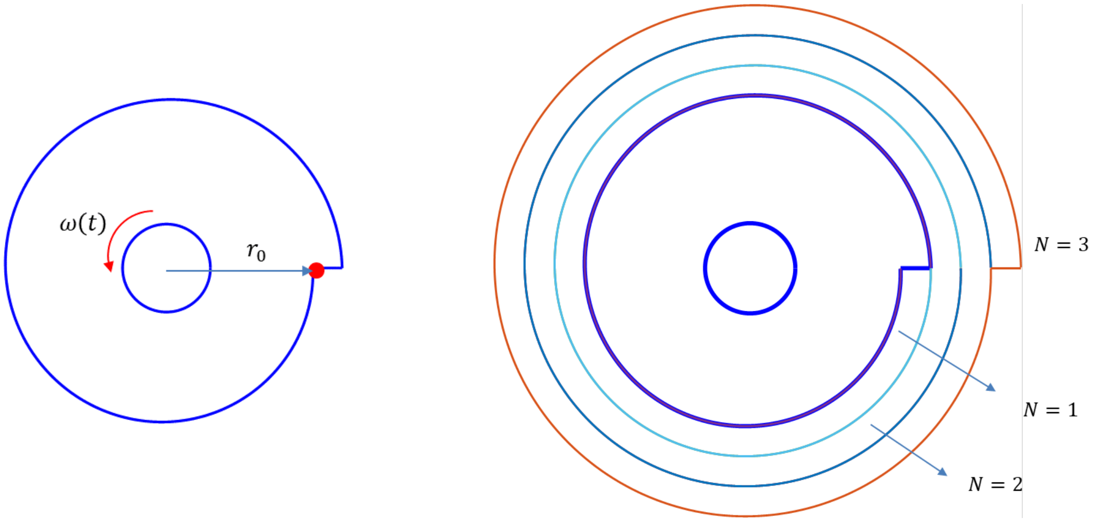

(a) Material spool

(b) Material spool with three layers of prepreg.

Figure 24. Material spool design.

Equations 11 presents relationships governing prepreg kinematics.

$$\begin{gathered} \omega(t) = \dot{\theta}(t) \\ Surface\ linear\ speed = v(t) = r(t)\omega(t) \end{gathered} \tag{11}$$

From equation 10, the relationship describing instantaneous prepreg surface radius can be derived:

$$r(t) = r_0 + \int_0^{\Delta t} \frac{h}{2\pi} \omega(t)\, dt \tag{12}$$

Equations 11 and 12 should be solved simultaneously to find the instantaneous radius.

$$r(t) = r_0 + \int_0^{\Delta t} \frac{h}{2\pi} \frac{v(t)}{r(t)} dt \tag{13}$$

Equation 13 is a recursive integral. It is noted that during the process, $v(t)$ is typically needed to be controlled. In other words, prepreg linear speed (payout speed or peel speed) must be controlled. Equation 13 calculates the instantaneous radius that is required to control the motor rotational speed to produce the required $v(t)$. The control system calculates this integral numerically to find $r(t)$.

It is also useful to continuously monitor the length of the material disposed or rewound during the process. The general equation of the spiral describing this geometry is:

$$r(\theta) = \frac{h}{2\pi} \theta \tag{14}$$

The initial diameter of the prepreg spool (i.e. diameter of the empty spool) is known and denoted by D_0. The final spool diameter can be measured after the spool is prepared to be used in the simulator, and it is denoted by D_1. The θ producing D_0 and D_1 can be found from substitution in 14.

$$\begin{gathered} @D_0 \rightarrow \theta_0 = \frac{\pi D_0}{h} \\ @D_1 \rightarrow \theta_1 = \frac{\pi D_1}{h} \end{gathered} \tag{15}$$

Curve length in polar coordinates is calculated using Equation 16.

$$L(\theta_0, \theta_1) = \int_{\theta_0}^{\theta_1} \sqrt{\rho^2 + \left(\frac{d\rho}{d\theta}\right)^2}\, d\theta = \frac{h}{2\pi} \int_{\theta_0}^{\theta_1} \sqrt{\theta^2 + 1}\, d\theta \tag{16}$$

The exact solution of Equation 16 is presented in Equation 17 which calculates available roll length at any given outer diameter, D_1.

$$\begin{gathered} L(\theta_0, \theta_1) = \frac{h}{2\pi}\left(\frac{\theta_1}{2}\sqrt{\theta_1^2 + 1} + \frac{1}{2} ln\left(\theta_1 + \sqrt{\theta_1^2 + 1}\right) - \frac{\theta_0}{2}\sqrt{\theta_0^2 + 1} \right. \\ \left. - \frac{1}{2} ln\left(\theta_0 + \sqrt{\theta_0^2 + 1}\right)\right) \end{gathered} \tag{17}$$

Different approximate methods also exist for estimating the rolled length. Two of these methods are reviewed here (Figure 25) and will be used when appropriate. The first method (a) compares the material surface area in the rolled (a hollow circle) and unrolled (a long rectangle) configurations. Length can be found by equating the two surface areas.

$$L = \frac{\pi}{4}\frac{1}{h}(D_1^2 - D_0^2) \tag{18}$$

The second method (b) assumes the spiral is comprised of a series of concentric circles, and the thickness of each circle is equal to the material thickness. The approximate number of turns, i.e. the total number of circles is $N = (D_1 - D_0)/2h$. The total length of material used to produce this configuration is the sum of circumferences of all the circles: $\sum \pi(D_0 + 2(i-1)h)$ where i varies from 1 to N. This series can be further simplified, which is presented in Equation 19.

$$L = \pi N\big(D_0 + h(N-1)\big) \tag{19}$$

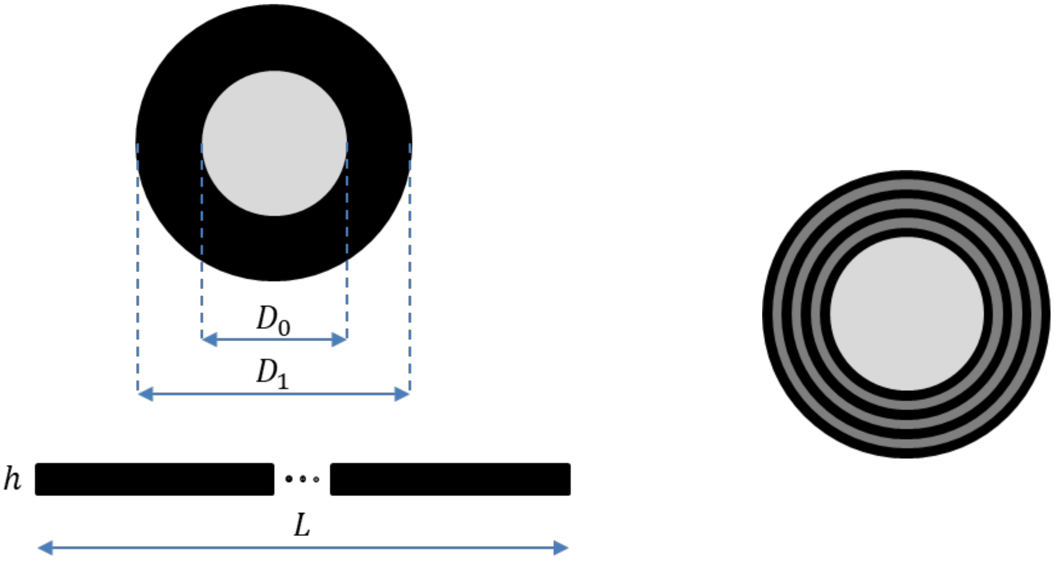

(a) Unrolled length **(b) Concentric circle approach**

Figure 25. Approximate methods for estimating rolled length.

4.1.2. Design of the Gantry System

Generally, robotic arms and gantry systems are used to produce layup trajectory and transfer the dispenser in AFP processing. As the speed and force/payload requirements increase, size and cost of robotic arms increase rapidly. Moreover, their control is often more complex. Therefore, a gantry-based system will be used to provide motion for the table-top simulator.

The payload of the system is estimated to be 8-10 kg. Up to 500 N force is applied by the compaction system and its reaction should be supported by the gantry. Moreover, the system is designed to achieve speed of 1 m/s over a travel range of 600 mm. This may result in significant dynamic forces during acceleration and deceleration of the system that need to be considered for gantry design.

The table-top gantry systems can be built from linear axes. ‘Linear axis’ typically refers to an assembly that includes a mechanism for transferring linear motion (e.g. belt and pulley, or lead screw and nut) and a mechanism for supporting the external loads (e.g. shaft and linear bearing, or carriage and guide rails for more heavy duty applications). A wide range of potential solutions, from designing and building the gantry from basic equipment, to designing and choosing an off-the-shelf linear axis from different manufacturers were considered at this stage.

Through an iterative process, the Festo ELGC-TB series was found to be a good solution for this application. This linear axis uses recirculating ball bearings as a guide, and a toothed belt system provides the drive for the carriage of the axis. The toothed belt mechanism’s repetition accuracy is ±0.1 mm. Off-the-shelf fixtures and mounting plates are offered for this specific series, for improved connectivity of these axes, in order to create various types of gantry assemblies. Maximum speed and accelerations supported by this axis are 1.5 m/s, and 15 m/s^2.

The linear axis must support the inertia forces of moving the payload and compaction force over a bridging span of ~600 mm. This can produce large moments around x-axis (M_x - see Figure 26, a). As the moment capacity of the commercial axes increase, cost of the system increases rapidly as larger and stiffer designs would become necessary. The load capacity of the system has been the deciding factor in choosing the ELGC series. Maximum permissible forces and torques (strength limits) on the ELGC-80 slides used for the simulator are presented in Table 2.

The loading applied to these linear slides is three-dimensional and quite complex. In addition to the maximum loads listed in Table 2, a load factor is defined that takes into account the three-dimensional nature of the loading (Equation 20). The terms in the equation’s numerators are the forces and moments applied to the guide, and the terms in the equation’s denominator are linear slide’s capacity for a 5000 km life cycle. If the value of the load factor exceeds 1, the total life cycle of the system will be reduced and should be found following Figure 26, b.

$$f_v = \frac{|F_y|}{Fy_{max}} + \frac{|F_z|}{Fz_{max}} + \frac{|M_x|}{Mx_{max}} + \frac{|M_y|}{My_{max}} + \frac{|M_z|}{Mz_{max}} \leq 1 \tag{20}$$

Table 2. Strength limits of the slides and bearings [23].

Parameter	Unit	Slide’s Strength Limit	Bearing Capacity for a service life of 5000 km or 5×10^6 cycles
Fy_{max}	N	900	5543
Fz_{max}	N	2700	5543
Mx_{max}	N.m	59.8	59.8
My_{max}	N.m	56.2	56.2
Mz_{max}	N.m	56.2	56.2

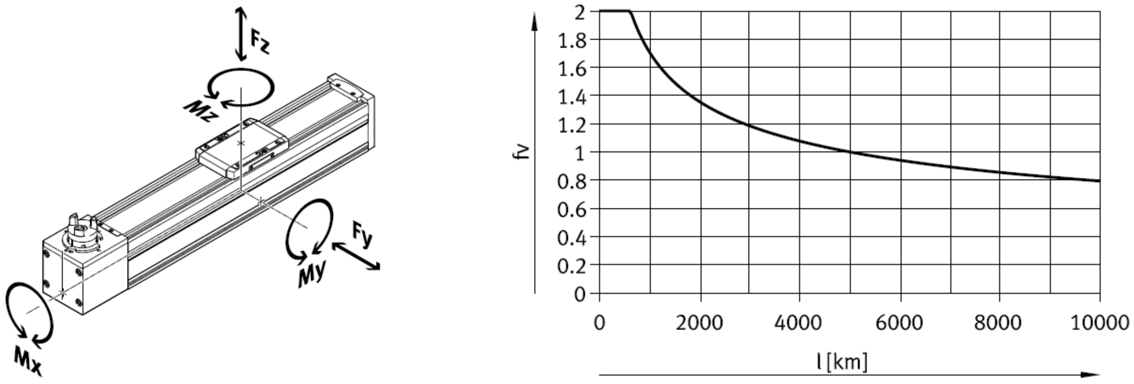

(a) Slide's moment naming convention **(b) Slide's service life**

Figure 26. Naming convention and service life of the linear axis [23].

In consultation with Festo's Application Engineering support, it was decided to use a single driven axis in the rail direction (x-axis) of the gantry (see Figure 27 for definitions of the bridge and rail axes). The other rail axis is a passive mechanism that only provides structural support. The bridge axis slides freely on the passive rail axis (Figure 27). This reduces from complexity of synchronizing two motors on both rail axes which could result in unwanted stresses on the entire body of the bridge axis with slightest mismatch between the two active rail slides. Moreover, available motors are easily able to carry the payload individually, so using two motors for the rail axis would not be necessary.

Festo Positioning Drives software helps with defining the system's duty cycles, calculating load factors resulting from dynamic forces of acceleration/deceleration on each slide, calculating load factors of the axis (along the axis, i.e., the thrust force) on each slide, as well as, calculating and choosing motors and drives for the application. However, there are not any features that allow the software to analyze forces produces inside the payload. More importantly, the software does not perform gantry kinetic analysis. It only considers effects of a concentrated mass located at a known distance (in the 3D space) from the free stage of a linear axis. Therefore, some manual analysis is necessary to ensure design safety.

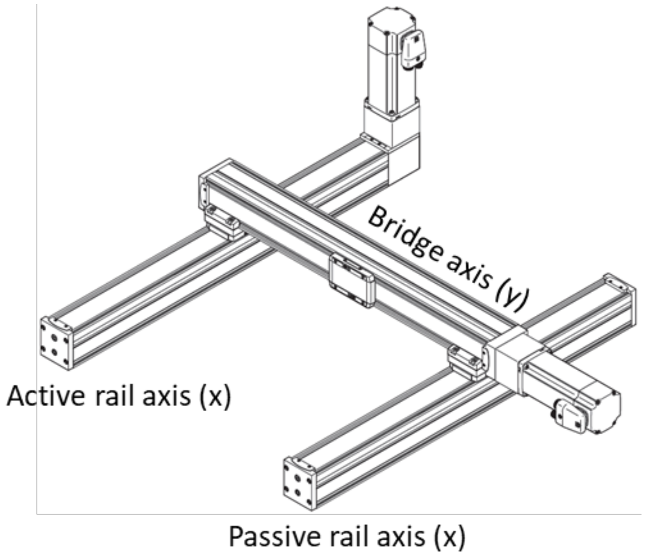

Figure 27. Proposed planar gantry layout.

Procedure for sizing of the linear axes. Three types of forces will act on each linear axis:

1. Gravitational forces
2. Inertia forces due to acceleration/deceleration
3. External forces

Maximal duty cycle of the system that is used for all simulations is presented in Figure 28. In order to determine the forces acting on stages of the rail axes, Euler-Bernoulli beam analysis should be performed on the bridge axis (Figure 29) to calculate the reaction forces. Assuming ELGC size 80 is used for the bridge axis, the total payload to be supported by the rail axes increases to ~15 kg (this is the final payload estimate used to size the rail axes after a few iterations which includes weights of the dispenser, the final bridge axis slide, and the final bridge axis motor).

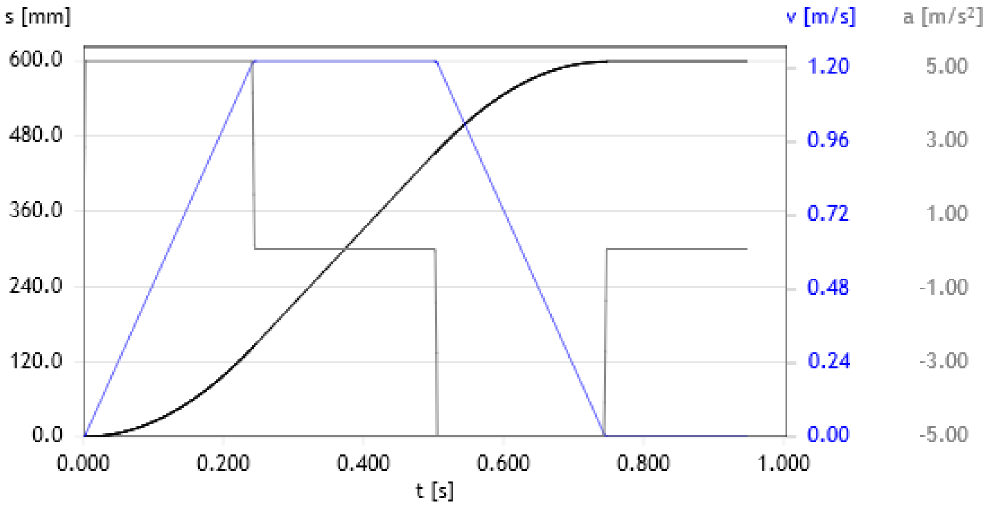

(a) Deposition motion profile

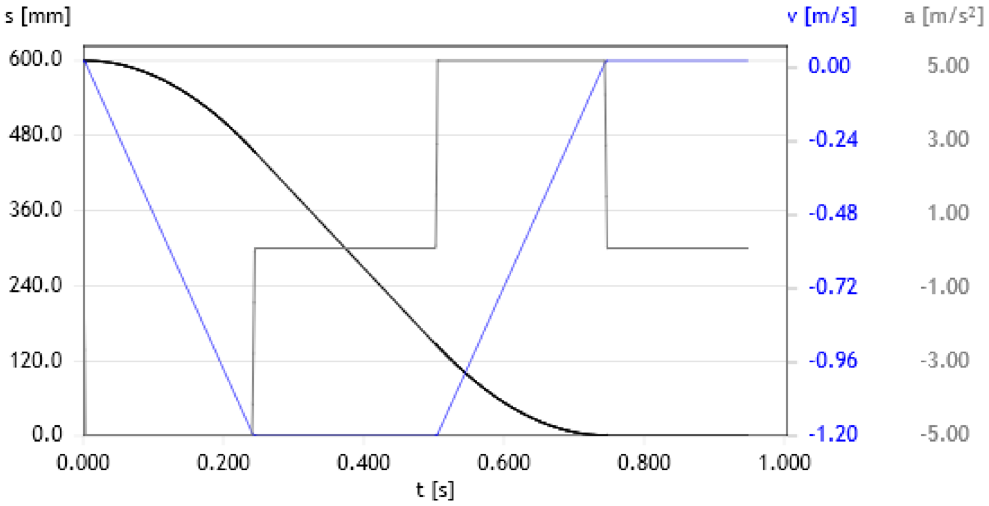

(a) Peel motion profile

Figure 28. Gantry's maximal effort motion profiles.

For a beam fixed at both ends under combined concentrated force, F, and uniformly distributed load, w, (superposition of Figure 29, a and b), the reaction force and moment at support A is given by Equation 21.

$$R_A = \frac{(3a + b)b^2}{L^3}F + \frac{1}{2}wL \tag{21}$$

$$M_A = -\frac{ab^2}{L^2}F - \frac{1}{12}wL^2$$

Force capacity of the linear axis is 15 times larger than its moment capacity, so the limiting factor, namely, the moments are investigated more closely. Moment at support A is maximized when $a = L/3$ and its peak value is equal to $\frac{1}{12}wL^2 + \frac{4}{27}FL$. The software merely considers effects of a moving mass from a specific distance, which results in moment arm of Fd (where F could be the force of gravity mg, or the force of inertia ma). The effective distance of the concentrated force acting on the bridge axis, for performing rail axis calculations in the software is $d_{c,e} = 4L/27$. The effective distance of the uniform load acting on the bridge axis, for performing rail axis calculations is $d_{u,e} = L/12$. The dispenser is considered to be a concentrated mass of 8 kg located at a distance of ~90 mm, and rail is a uniform load with the mass of 7 kg located at a distance of 50 mm. By using the effective distance values for a mass/moment-arm analysis, the resulting moments will become equivalent to beam-based analysis of the gantry system. Using, ELGC size 80 for the rail axes results in the load factor 5% and 18%, respectively. Load factor resulted from the compaction force is calculated manually and found to be 74%. Therefore, the total load factor of the ELGC 80 used for the rail axes is 98%. This means if the gantry system constantly operates under the worst-case scenario condition, the design is safe, and the service-life is at least 5×10^6 cycles. The worst-case scenario condition is defined as continuous operation of the system under the maximal effort motion profiles (at the speed of 1.2 m/s, Figure 28), while 500 N compaction force is applied, and dispenser is located 20 cm away from one of the rail axes. It is interesting to note that using compaction forces of 300 N and 400 N results in load factors of 67% and 82%, respectively. The same ELGC size 80 linear axis is used for the bridge axis of the gantry too, since there are not any considerable benefits in using the smaller size.

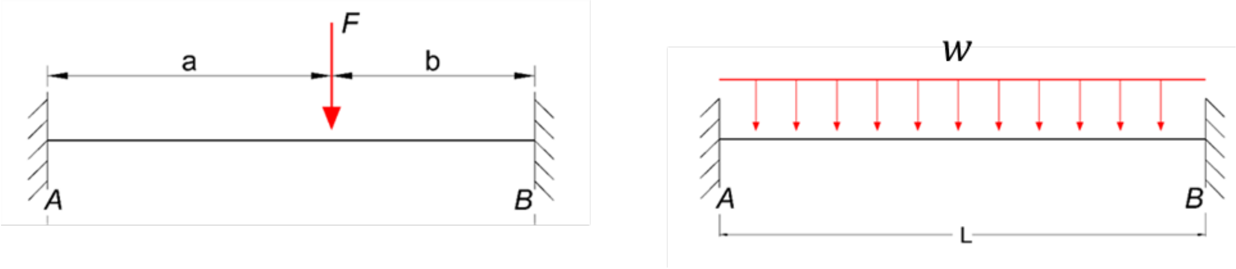

(a) Concentrated load **(b) Distributed load**

Figure 29. Bridge axis as a double-fixed beam.

Procedure for sizing of the motors and drives. The same maximal effort motion profiles presented in Figure 28 are used to simulate the workload of the motors and drives. Again, the limiting factor for motor sizing is the inertia ratio of the system. The available electrical power system in CRN laboratories is 208 V AC three-phase. This was defined in the software to receive potential motor/drive combinations that are compatible with the available infrastructure. The entire payload was simulated to be driven by a single axis. Payload is located furthest from the active axis, to simulate maximal loading condition on the motor. The EMMT-AS-100-L-HS-RM motor and CMMT-AS-C5-11A-P3-EC-S1 drive were chosen for the rail axis. This motor/assembly results in inertia ration of 8 which is acceptable and has room for future expansion of the system.

The same process was followed to size the motor and drive used for the bridge axis, except the payload for this axis is only 8 kg (the estimated weight of dispenser). EMMT-AS-80-H-HS-RM motor and CMMT-AS-C3-11A-P3-EC-S1 drive were chosen for the rail axis. The inertia ratio for this motor/assembly is 6. The EC noted in the name of both drives used, indicate they use EtherCAT technology to communicate the main controller; hence they are compatible with the control system architecture used (see Section 4.1.3). The final CAD model of the planar gantry system is presented in Figure 30.

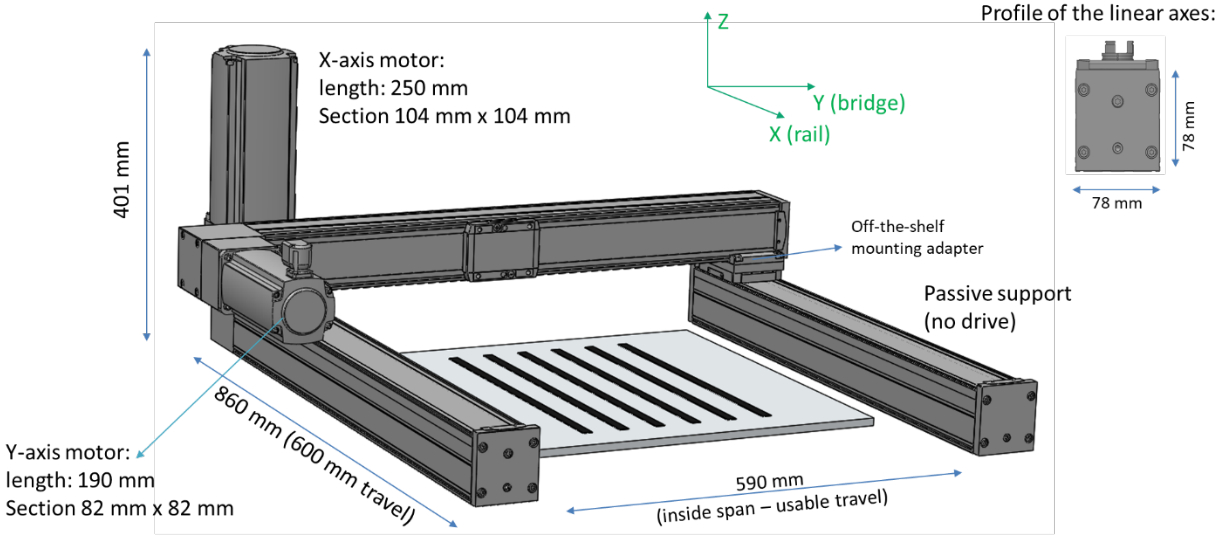

Figure 30. CAD design of the gantry.

4.1.2.1 Tool Setup

T-slot fixture plates are used to have a fast and versatile method for tool replacement. The fixture plates and the gantry system are mounted onto a wooden base for increasing stability and mobility of the system.

One of the most influential parameters on tack is temperature. Therefore, it is crucial to have the ability to control layup temperature, not only during deposition, but also during peel and dwell time. Heating blankets are used to control tool temperature independent of deposition temperature. The heating blankets are sandwiched between the tool (on the top) and an insulator (on the bottom). The insulator prevents the heat to be lost into the fixture plate and allows for a more efficient heat transfer in the tooling system. Figure 31 shows schematic drawing of the front view of the tool setup.

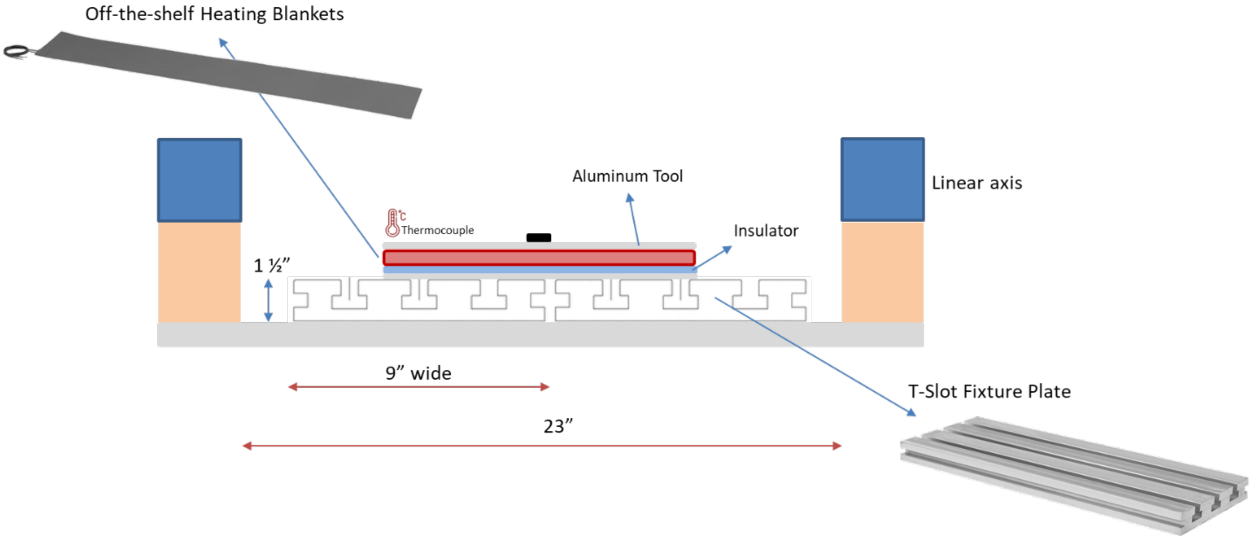

Figure 31. Front view schematic of the tool and gantry setup.

4.1.3. Design of the control and electrical systems

The primary objective is to choose an industrial grade control system that is a highly reliable, repeatable, and deterministic system to produce high quality data. A modular design that can be easily expanded in future is favored. The Beckhoff automation platform was chosen for this reason. The architecture of the system is presented in Figure 32. An Industrial PC (IPC) is used as the main computer/processor of the control system. Various different input/output modules are offered from Beckhoff that can be added to the IPC for controlling processes or receiveing data. All equipments are controlled centrally and all the sensor data from the AFP simulator are gathered in the IPC. EtherCAT technology is used for realtime communication between all devices.

All the control system modules are shown in Figure 33 in the specific order designed to be implemented (from left to right). Their name and a brief description of their function in the system are presented in the images. All electronic devices required for equipment used, including switches, contactors, overcurrent protection devices (e.g. fuses and circuit breakers), surge protection devices and wire sizings are designed according to the Canadian Electrical Code, Part I (2018) and CSA C22.2 No. 286-17 (industrial control panels and assemblies). A 72 x 36 x 18in (Height x Width x Depth), IP55 enclosure was purchased and modified (Figure 34) to install all components of the electic and contorl system assembly inside of it.

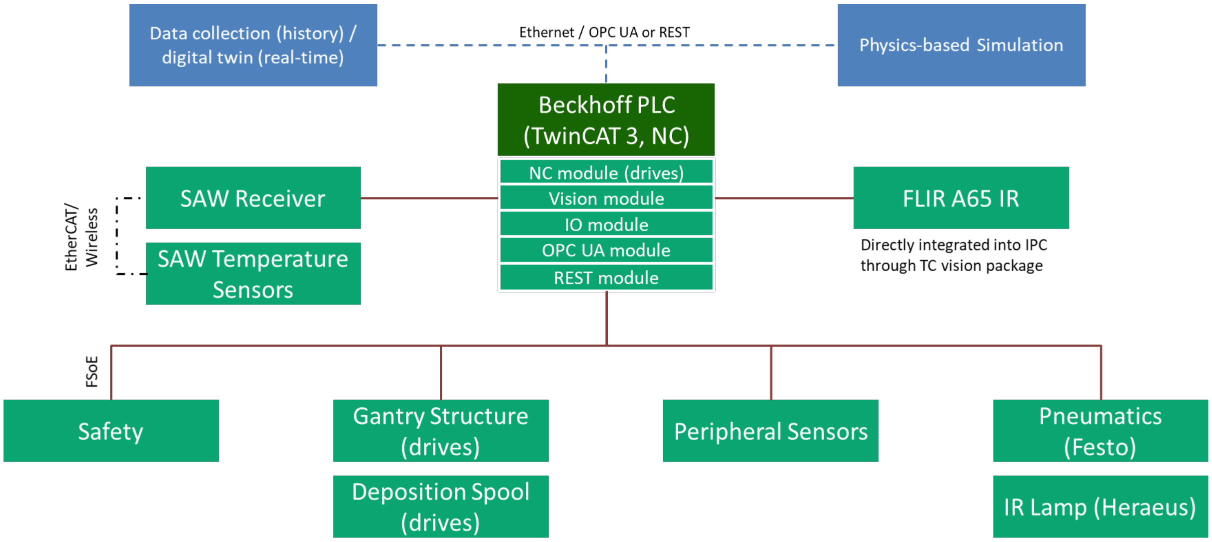

Figure 32. Architecture of the automation platform.

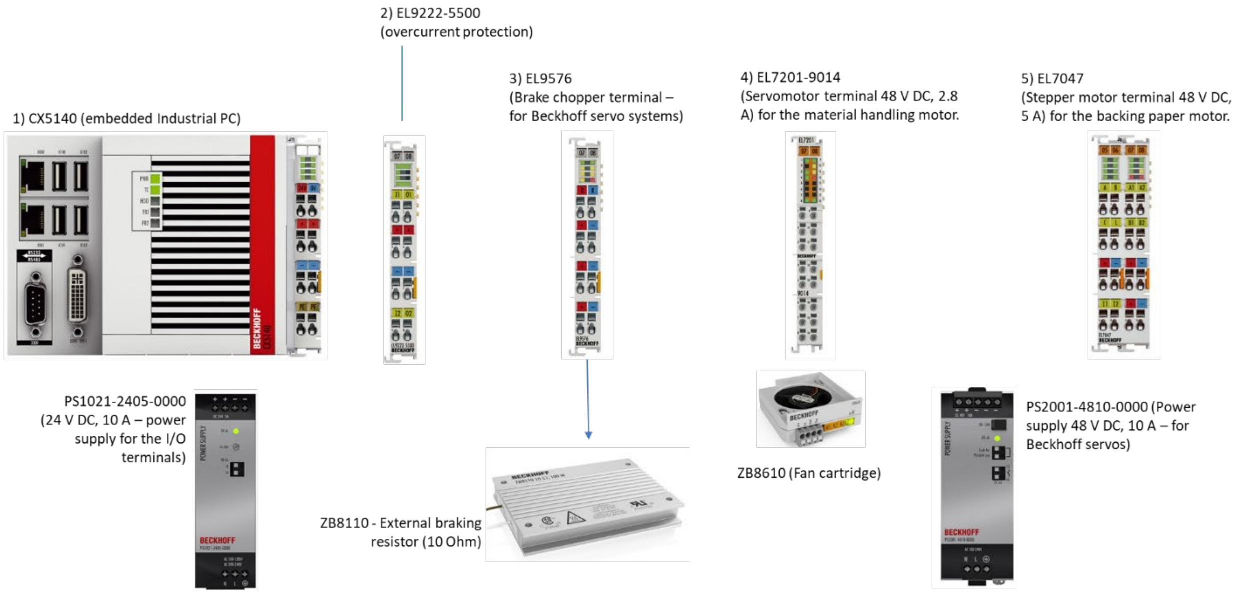

(a) Control system modules.

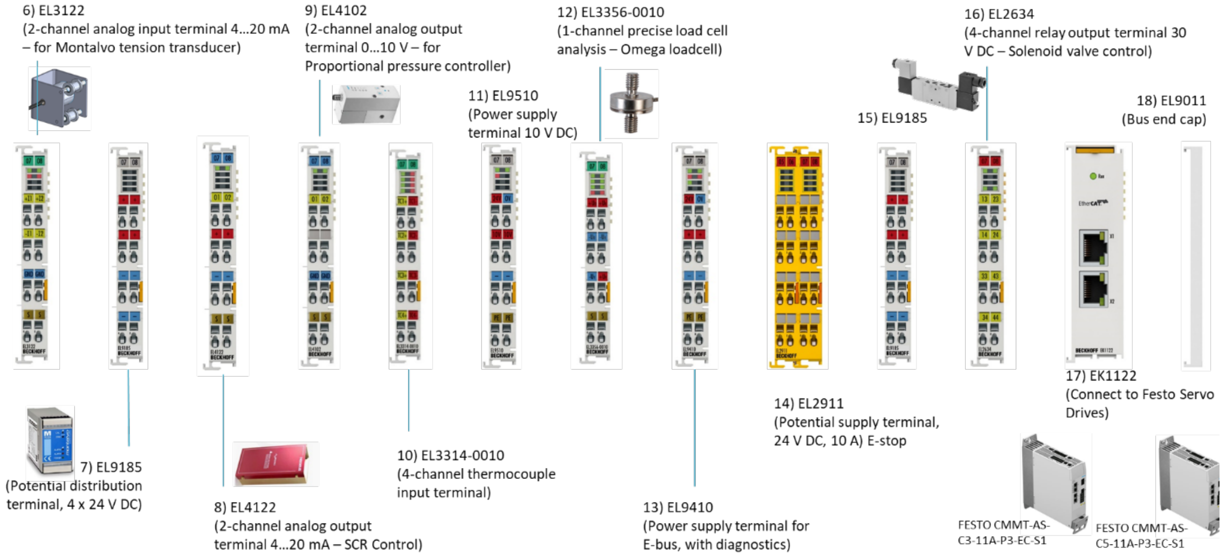

(b) Control system modules; continued.

Figure 33. Control system modules and their functions.

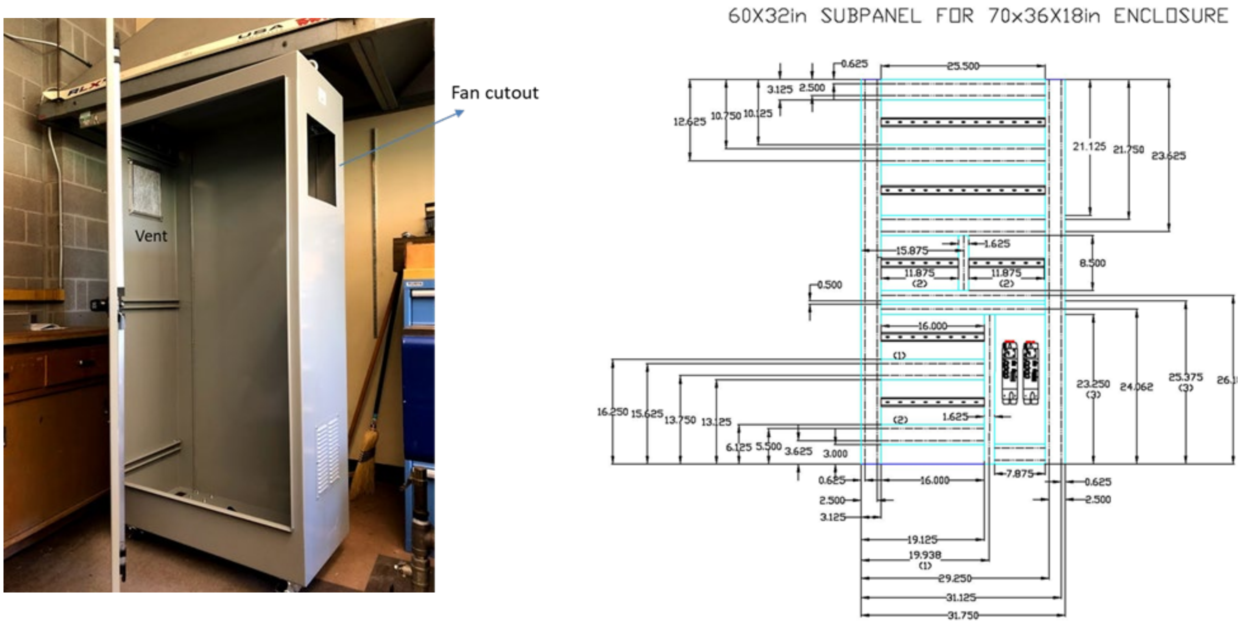

(a) Control system enclosure **(b) Enclosure's subpanel design**

Figure 34. Control system assembly.

4.1.4. Summary

Details of the different sub-systems involved in the AFP cell were presented in section 4.1. Various design considerations were discussed, and the overall procedures and results of equipment sizing were presented. Figure 35 shows the latest drawing of the complete system assembly and a closer view of the dispenser.

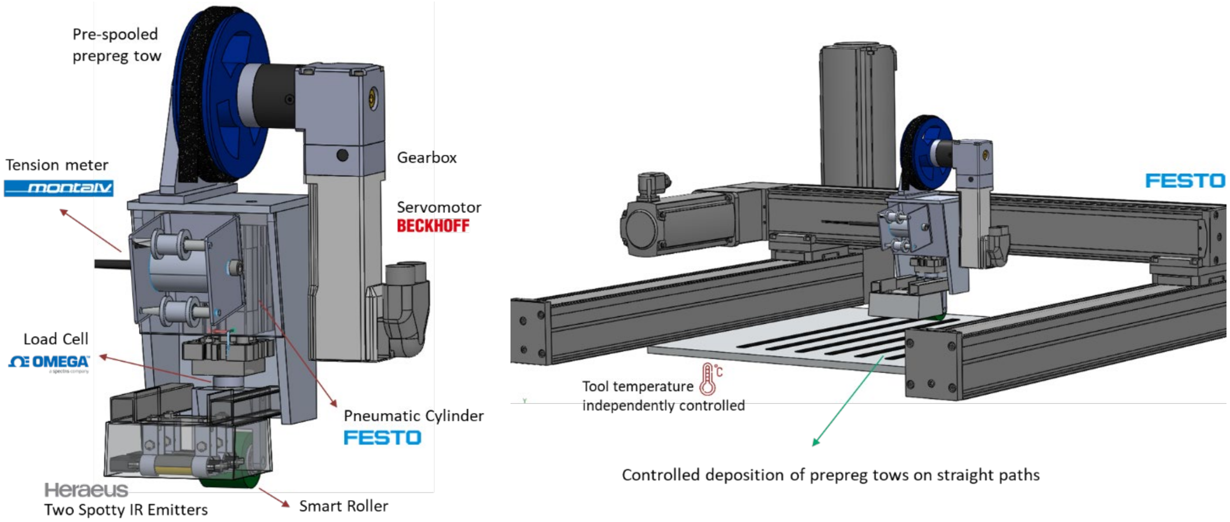

(a) Dispenser **(b) Complete AFP Cell**

Figure 35. AFP Simulator.

4.2 Sense

One of the objectives of the present work is to identify which material and process parameters are most pertinent to the AFP process outcomes and can provide the most useful information. The smaller scale and high flexibility of the simulator developed within the scope of this project allows for performing comprehensive measurements throughout the system. Producing a state of ‘over measurement’ at this scale enables the researchers to identify the most crucial parameters that need to be monitored in the industrial AFP process. The following describes the first set of standard sensors that are implemented in the system. Moreover, efforts to develop the first operational version of a smart roller, used to measure local pressure at the nip point of the process, are presented.

4.2.1. First set of Standard Sensors

A FLIR infrared temperature camera sensor is used to monitor the full temperature history of the entire layup. Thermocouples are used to perform spot temperature measurements. Moreover, they provide temperature of the tooling to the control system which allows the IPC to perform closed loop temperature control for the tooling. SAW- (Surface Acoustic Wave) based temperature sensors may be used, as needed, to perform accurate and continuous temperature measurement of critical areas. SAW sensors are wireless, which allows access to hard to reach areas without surface interruption (e.g. via embedding them in the prepreg substrate).

An axial tension/compression load cell (Figure 36, a) from Omega is used to monitor and control the AFP compaction force, i.e., the force output of the pneumatic cylinder.

A precision tension transducer (Figure 36, b) from Montalvo is used to continuously measure prepreg tow tension during the process. This sensor utilizes a N-Micro loadcell, capable of measuring the radial force applied to the transducer. Tow tension is then calculated through the geometric relationship between the loadcell and idler rollers, as defined in the tension transducer packaging. The rollers used in this sensor feature an anti-adhesion coating which facilitates frictionless transmission of prepreg tows with minimal buildup of resin over time.

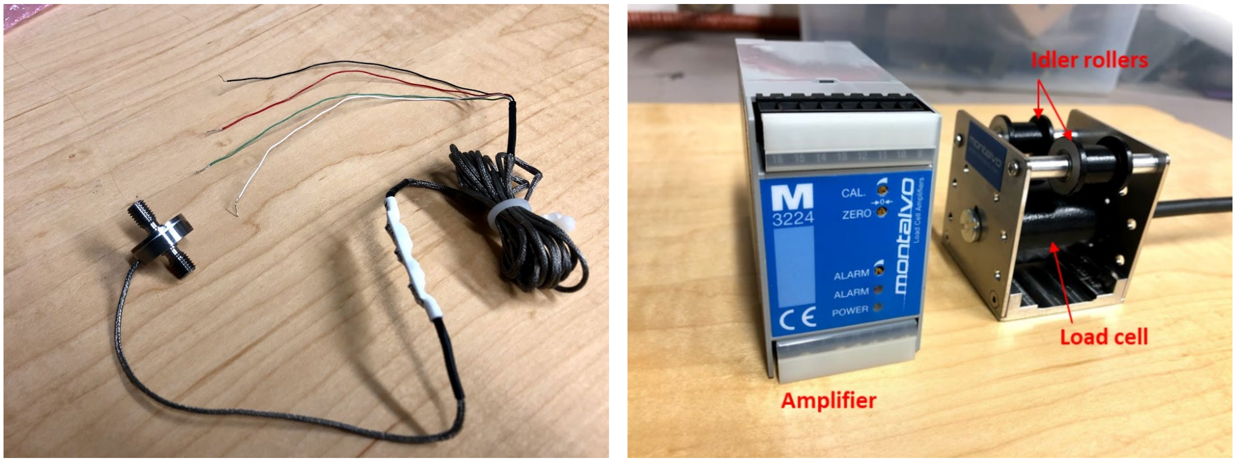

(a) Tension/compression sensor **(b) Precision tension transducer and amplifier**

Figure 36. Force sensors.

Previous research suggests some of the process-induced defects initiate in the proximity of the nip point and as a result of the tow-roller interactions. It is necessary to monitor the prepreg behavior near the nip point, to illuminate the mechanics of these interactions. Therefore a video camera is used to record prepreg movement during deposition.

4.2.2. Smart Roller

During the AFP process, a compaction roller is used to conform the prepreg tows onto the tool surface. The primary functions of compaction rollers in the AFP of thermosetting prepregs is to place the prepreg tows, facilitate the development of required levels of tack, and to keep the voids between prepreg tows as small as possible. The perfect condition is a fully compacted and void-free lay-up [24],[25].

Typical AFP processes use global parameters, such as the total compaction force applied to the roller, and the overall temperature profiler before or after deposition, to monitor the process. These same global parameters are then used to interpret process quality outcomes. On the other hand, defect formation during prepreg deposition is inherently a local process. Hence, the variability of process conditions and their measurements cannot be ignored. When prepreg tow is placed on the tool surface, it is necessary to measure local relevant information at the nip point of the process.

A smart roller has been developed using flexible sensor technology that is able to measure process parameters at the nip point of the process. Sections 4.2.2.1 and 4.2.2.2 review the fundamentals of these sensors, as well as, development of the first operational version of the smart roller. In addition to the sensing features, it is equally important for the roller to match or surpass the mechanical performance of industry-standard rollers in compaction. To this end, a survey of the open literature is performed to investigate what parameters drive the compaction roller’s performance in the AFP process.

4.2.2.1 Smart Roller: Introduction and Operating Principles

The overall objective of the smart roller development sub-project is to develop compaction rollers capable of measuring relevant process parameters at the nip point of the process in an in-situ manner. Three generation of rollers are foreseen. The first generation aims at quickly developing the capability to measure compaction pressure. While fast implementation is prioritized at this step, efforts are focused on proper resolution of the sensor, providing the required sampling rate, and covering the full range of pressures experienced in the process. In the second and third generations of the roller, the ability to measure shear stresses and tilt, as well as temperature will be targeted, respectively.

The smart roller technology uses flexible capacitive sensors to achieve the mentioned objectives [26]. A typical configuration of a sensor cell is presented in Figure 37. The sensor cell is comprised of two flexible electrodes and the space in between them is filled with a flexible polymer dielectric. The change in mutual capacitance between the two electrodes is then characterized and related to the state of stress. When the sensor cell is subjected to pressure (b), the normal distance between the two electrodes changes, changing the magnitude of capacitance which is related to the magnitude of applied pressure. On the other hand, the specific arrangement of the top layer of electrodes allows for sensing shear stresses. Upon subjecting the sensor to shear forces, the relative location of the top electrode changes (c), altering the distribution of capacitance. The magnitude of change in distribution of capacitance is then linked to shear stresses.

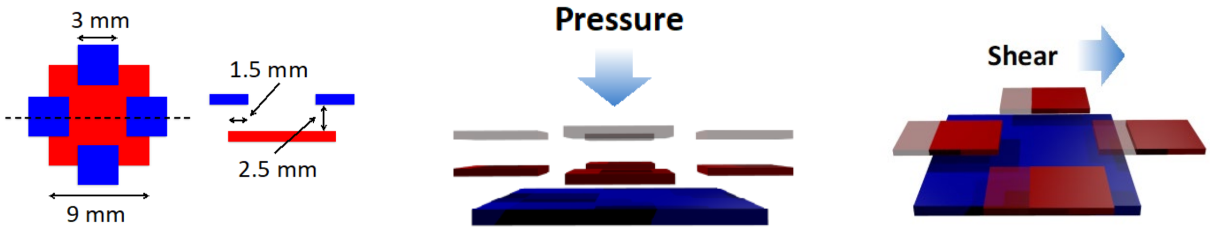

(a) (b) (c)

Figure 37. A typical sensor cell and its deformation under pressure and shear loading.

4.2.2.2 Smart Roller: Design

The present roller consists of an external shell, and a central hub (for mounting onto the roller axel). There is ample space between the hub and the shell to accommodate sensor electronics and a battery (Figure 38, a). These two components are three-dimensionally printed out of PLA. Once the smart roller design is finalized, the load bearing parts of the roller (e.g. shell, spokes, and hub) can be machined out of a stiff material such as aluminum or steel. Spokes are designed between them to provide structural support. A smooth opening is designed in the shell to allow for electrical continuity between the sensor installed on the shell's external surface and the electronics inside of the roller (Figure 38, b).

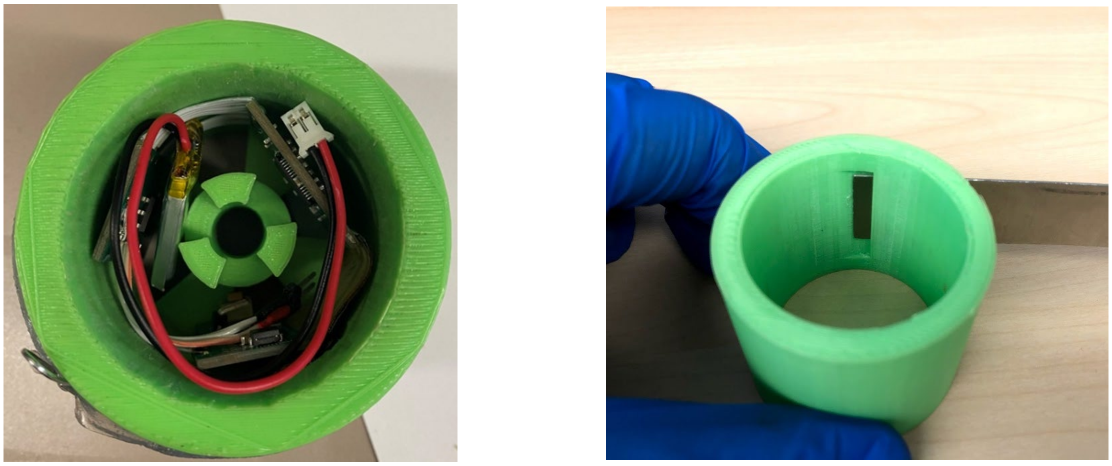

(a) (b)

Figure 38. Roller interior and exterior.

The current operating version of the roller is composed of a cross-grid array of electrodes.

Bottom electrodes are six copper traces designed on the flexible Printed Circuit Board. Top electrodes consist of three strips of black carbon embedded in a molded shore 00-30 Ecoflex substrate. Each cross-over point between the electrodes creates a taxel where capacitance is measured (Figure 39).

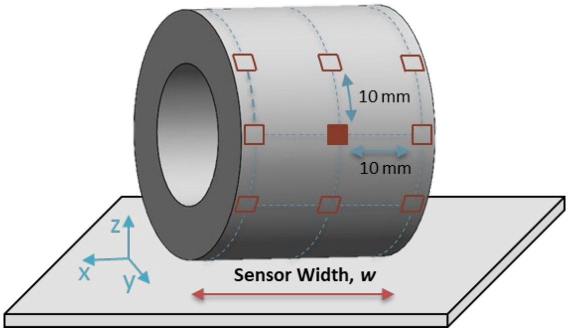

(a) Schematic of flexible sensors placed around the roller forming the roller tire. Each red square highlights a taxel as shown in figure b.

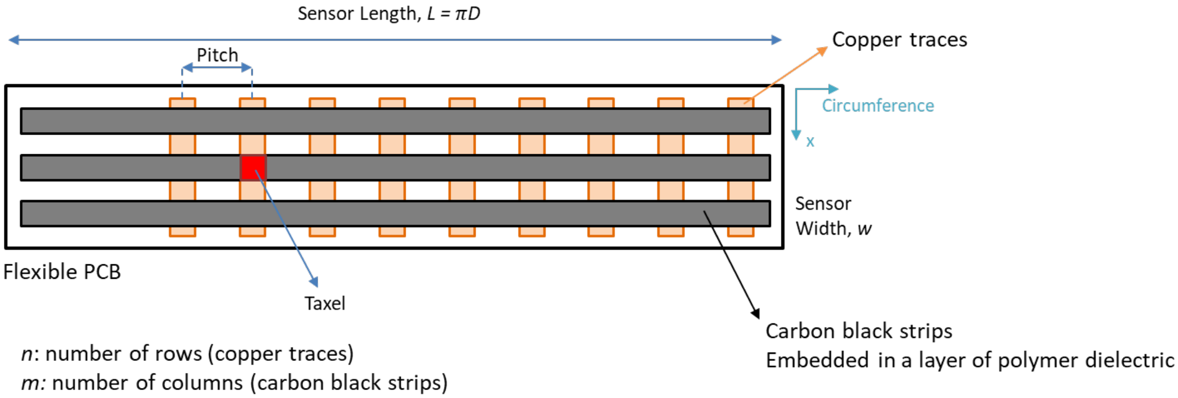

(b) Schematic of a flat sensor.

Figure 39. Schematics of the sensor.

The flexible sensor can be bent and adhered around the external roller shell. The completed sensor assembly, including flexible sensors and printed circuit boards, are presented in Figure 40. It is essential to note that the sensor is entirely wireless, enabling free spinning of the roller without any restrictions. A rechargeable battery is used to provide power to the internal circuitry, and Bluetooth communication is used between the sensor and the signal receiver. The completed roller assembly is presented in Figure 41.

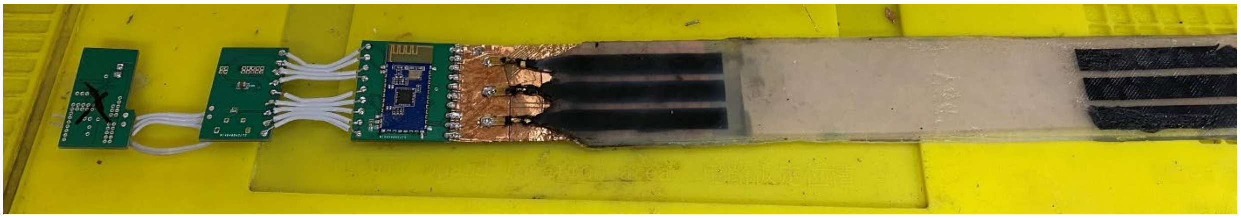

(a) Top

(b) Bottom

Figure 40. Completed assembly of the sensor.

(a) Roller assembly

(a) Roller assembly mounted on a temporary hand-held bracket.

Figure 41. Completed roller assembly.

Figure 42 (a) schematically shows the taxel distribution in the region of contact as the roller is rotating and moving forward and (b) shows the distribution of taxel output values in a bar chart. The (x, y) coordinates of the bar chart correspond to the spatial location of the taxels, x being along the contact width and y along the length of the sensor (i.e. circumference of the roller).

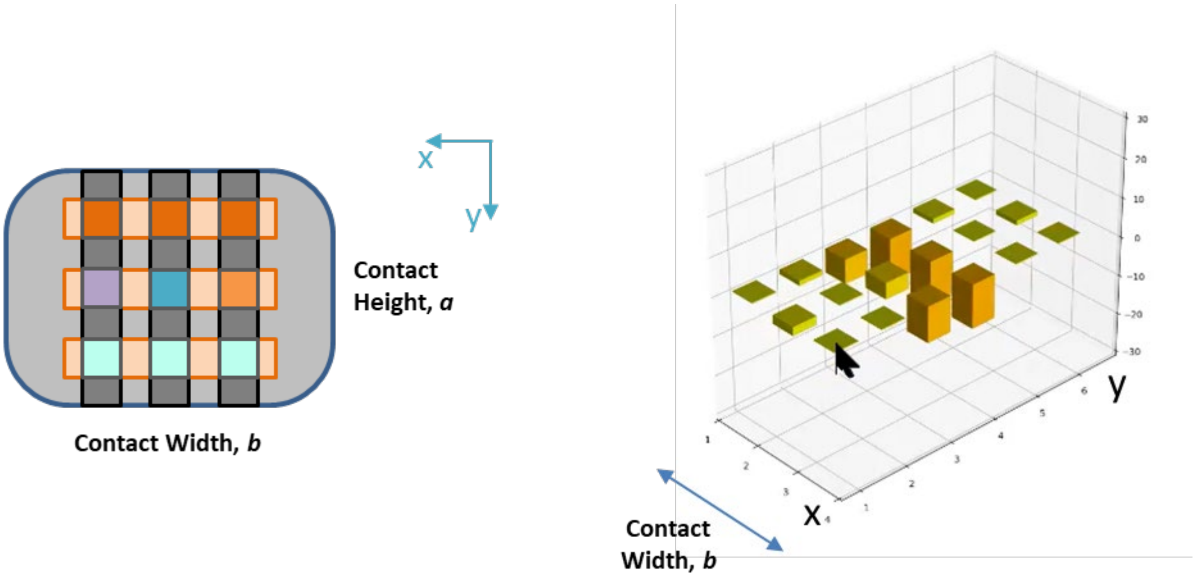

(a) Schematic of taxels in the contact region (i.e. process nip point).

(b) Bar chart plot of sensor output.

Figure 42. Smart roller contact region and measured output.

4.2.2.3 Roller Mechanical Performance: Background

A comprehensive review of the open literature has been performed to determine the parameters that drive the mechanical performance of the roller during prepreg compaction in the AFP process.

A number of patents exist on design of AFP compaction rollers. However, they are unanimously concerned with providing a uniform pressure when depositing multiple (up to 24-32) tows in a course. As the number of tows delivered in a course increases, the roller length must increase. If the roller is designed in a single part, there will be a large variation in compaction pressure distribution. Notably, prepreg tows located at the center of the roller will experience considerably larger pressures compared to those located at either end of the roller. In order to overcome this issue, segmented roller designs have been proposed. The roller is built from multiple segments, each one is as wide as the width of the prepreg tow used in the process and each segment is able to move independently. The independent movement of the segments produces a much more uniform and controlled pressure on all prepreg tows,

Two important segmented roller designs are reviewed here. Mischler et al. at Ingersoll Machine Tools Co disclosed a design providing a linear degree of freedom for each roller segment [27]. Each segment has a ball bearing to facilitate its rotation around the axel. Outside of the outer race of the bearing, roller's flexible cover is located. Inside of the bearing, an empty space exists which can accommodate the shaft and two bladders. This space allows each segment to move in and out independently upon actuation of the bladders with a pressurized fluid. Therefore, each prepreg tow can be compacted independent of the adjacent tows and roller segments.

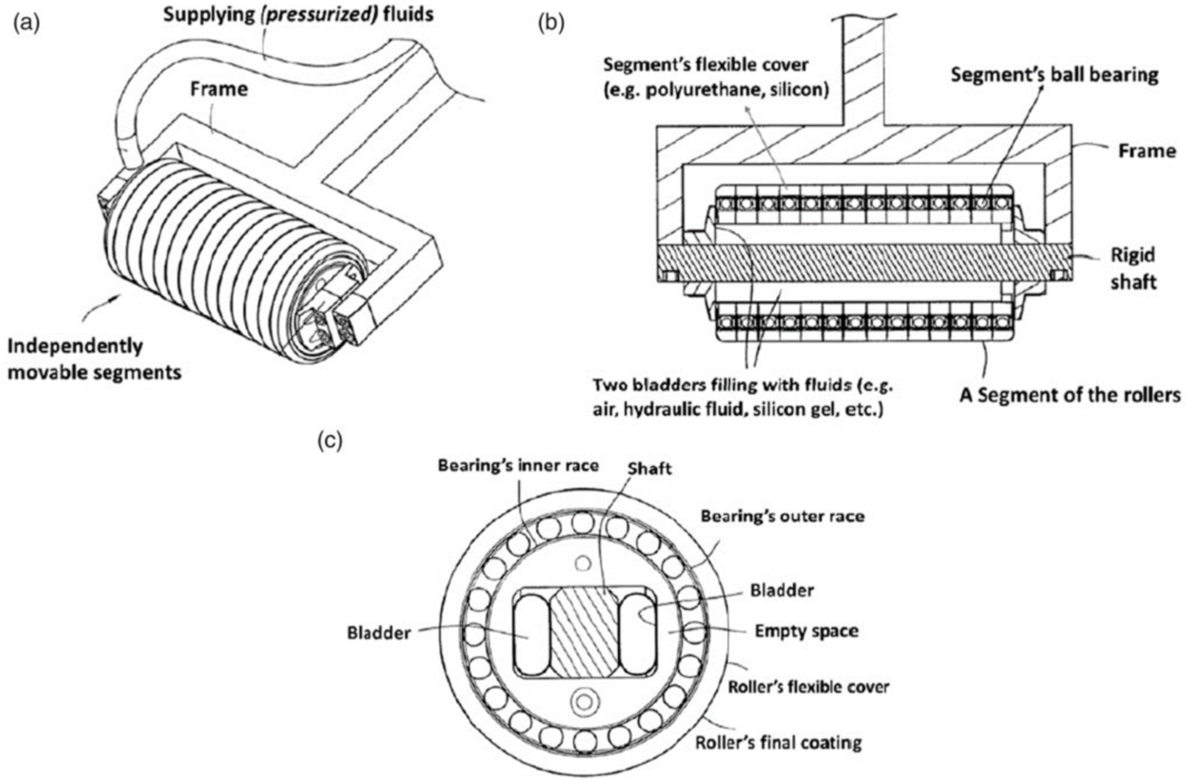

Figure 43. Segmented roller with linear degree of freedom [27].

One issue with the typical segmented rollers allowing for linear translation of segments is that they require a large physical envelope to allow for the linear displacement. There is a high possibility of collision between rollers and other machine components due to the highly constrained geometry. Johnson et al. at the Boeing Company [28] developed a conformal compaction roller which does not require the additional space needed by the linearly translating roller segment.

The compaction roller consists of multiple roller segments located side-by-side of one another (Figure 44). Each segment is supported for rotational movement about an eccentrically disposed pivot shaft. The bladder is located inside the bore, against a strong back member. When inflated with pressurized fluid, it causes the roller segments to rotate about the eccentrically disposed pivot shaft against the tool surface.

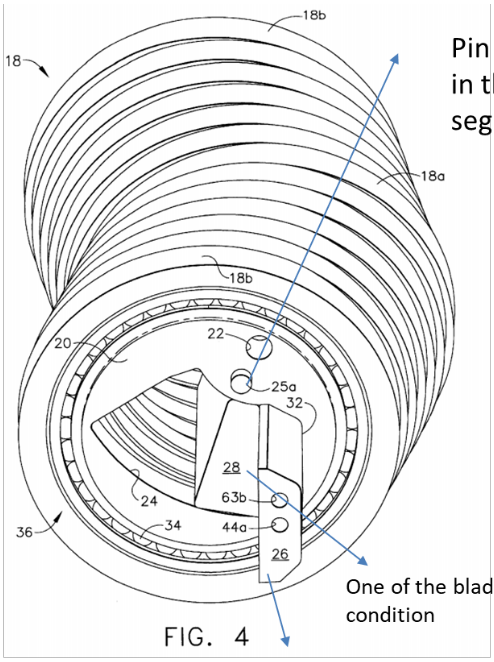

FIG. 4

Pin 25a only exists in the endmost segment.

One of the bladders in a relaxed condition

The strong back member is touching the aft edge 32 of the arcuate slot of an endmost one of the roller segments 18b, thus limiting movement of the of each of the roller segments 18 in the fore (i.e., to the left) direction.

Figure 44. Segmented roller with rotation degree of freedom [28].

While patents address the practical aspects of disposing large number of prepreg tows, most published papers investigate contact properties of the roller. Cheng et al. [29] considered contact characteristic of the compaction roller and morphological changes of prepreg under the compaction roller.

Jiang et al. [30] used finite element models to quantify pressure uniformity along the contact height (as defined in Figure 42, a). Then, they investigated effects of roller radii, material grade and width on pressure uniformity of a wide single-part roller capable of depositing 16 tows in a course. In a subsequent paper [31], they developed a theoretical contact model to obtain compaction pressure distribution during the dynamic tow placement process.

Chu et al. [32] examined the effect of pressure non-uniformity caused by nominally incomplete contact and proposed some restriction on placement geometry. Nominally incomplete contact is defined as when normal curvature of the tool changes along the center line of contact width. For example, when laminating a cylinder on a direction other than 90°, some changes in local normal curvature are observed (Figure 45).

Bakhshi and Hojjati [24] performed an experimental trial using multiple different rollers and under various process conditions. They qualitatively examined the effect of compaction roller grade and architecture on layup quality. Perforation patterns are sometimes used in AFP compaction rollers to enhance roller deformability. Potential effects of these patterns as well as material stiffness on layup quality were considered.

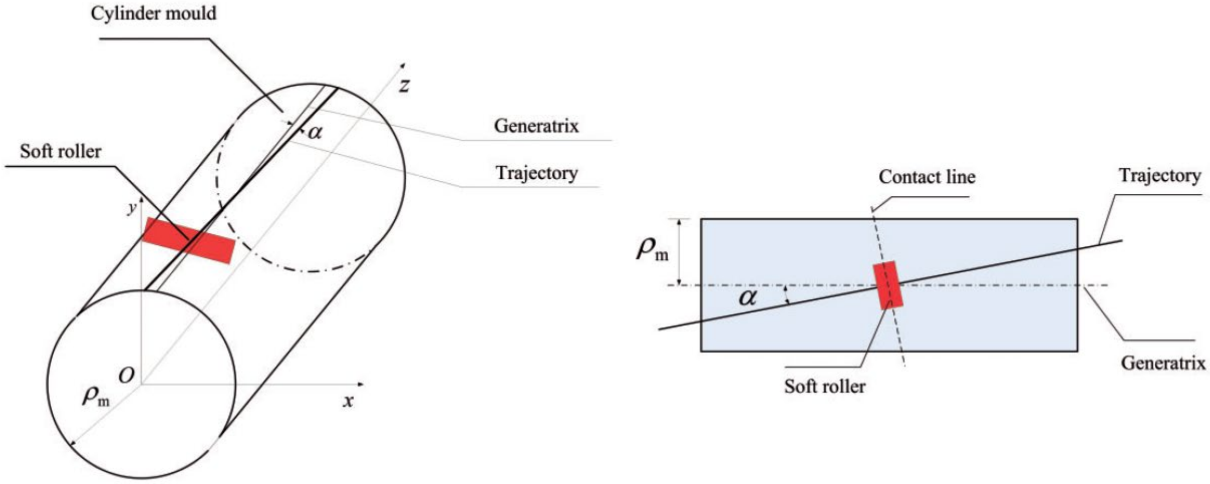

Figure 45. Geometrical relationship between trajectory and roller [32].

From a modeling perspective, even though finite element analysis of the roller may appear to be simple at first, this problem involves simulation of multiple nonlinear and complex physics. Overall, deformations are well into the nonlinear, large deformation domain. A roller is typically made up of soft, highly compliant nonlinear polymers, and it is in *contact* with deformable prepreg tows and a rigid tool. Moreover, AFP is a dynamic process; therefore, it may be necessary to simulate the entire pressure profile along the trajectory of deposition. Solving this problem fully requires significant computational resources.

This review suggests the majority of published academic papers have focused on two issues: i) developing theoretical models for roller contact characteristics; and ii) investigating the effect of particularly large roller width, on compaction pressure distribution and potentially its implications on layup quality. Industry, on the other hand, has addressed the second issue by changing the design of the rollers from a single-part design to the segmented designs. The segmented design allows compaction rollers to dispense a large number of prepreg tows with a higher degree of control over compaction pressure uniformity.

It appears that the starting point of roller design is typically the accumulated engineering experience and intuition, which is somewhat taken for granted. The fundamental question that remains to be answered is what are the parameters that drive and determine roller performance in the AFP process. For example, how are the optimal roller geometry and material properties defined? Certain geometrical constrains such as machine envelope or concave tool curvature exist that should be taken into consideration when designing the roller geometry. However, an important issue to be addressed for prepreg deposition is, what roller parameters optimize prepreg compaction, best facilitate tack formation, and pave the way to produce the highest achievable layup quality.

In order to approach AFP processing scientifically, one needs to explicitly consider the parameter that drive roller performance from perspective of the prepreg material being processed. Moreover, interactions of the roller with substrate and prepreg tows should be understood, and the influence of these interactions on layup quality need to be examined. Recent advancements in prepreg tack characterization as well as the insights offered by the physics-based models of AFP, can provide more specific requirements on roller specifications.

4.2.2.4 Roller Mechanical Performance: Approach

In this work, finite element analysis is performed using Abaqus to study contact properties of the compaction roller. A typical industry-used AFP roller is simulated to establish a standard baseline of performance. In the first step, it is aimed for the smart roller to replicate the contact properties of the standard baseline. Then, a larger investigation will be performed to address the fundamental questions discussed before. The aim this investigation is introducing the roller design technology to become part of the AFP parameters that need to be carefully considered and optimized in conjunction with the rest of the process window.

The baseline roller's outer and inner diameters are 38 and 20 mm, respectively. The material is a shore A 60 durometer polymer, with Young's modulus approximated at 5.5 MPa. Figure 46 shows the model and a typical deformation profile. A few important parameters to consider are the peak magnitude of compaction pressure produced by the roller and the overall distribution of the pressure over the area of contact, and the size of the contact region. Figure 47, presents the contact pressure distributions (CPRESS) at three different levels of compaction force applied to the roller.

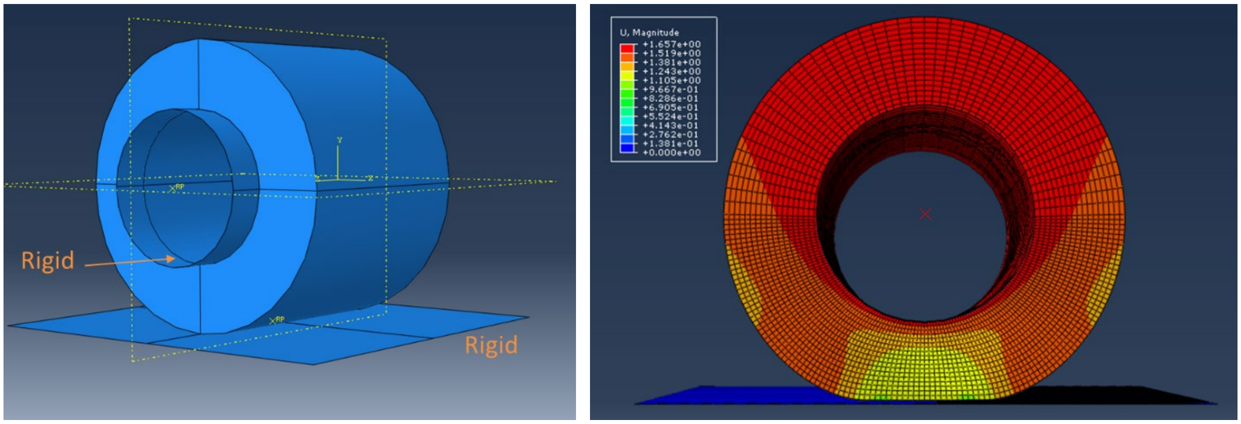

(a) Model of the baseline roller. **(b) Roller deformation profile (mm).**

Figure 46. Baseline compaction roller.

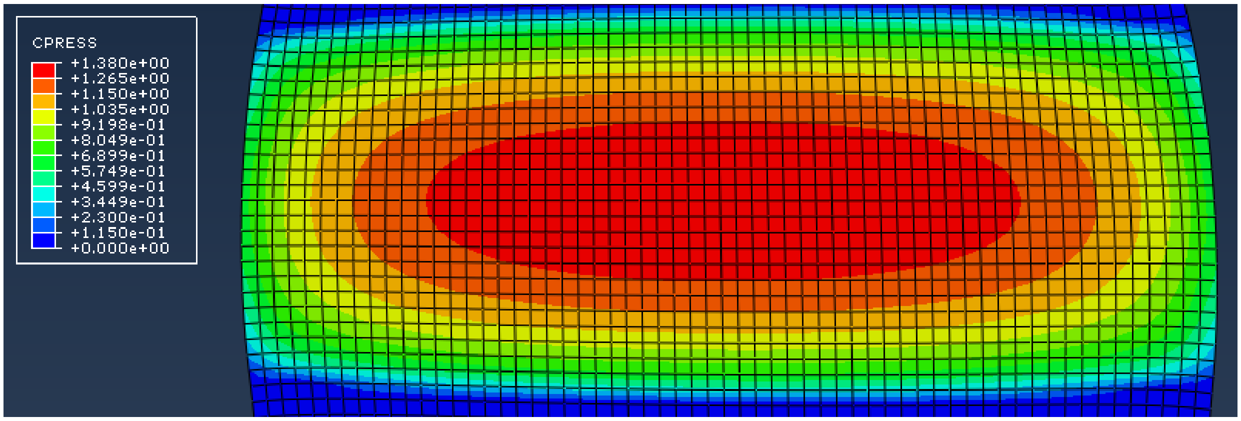

(a) F = 400 N

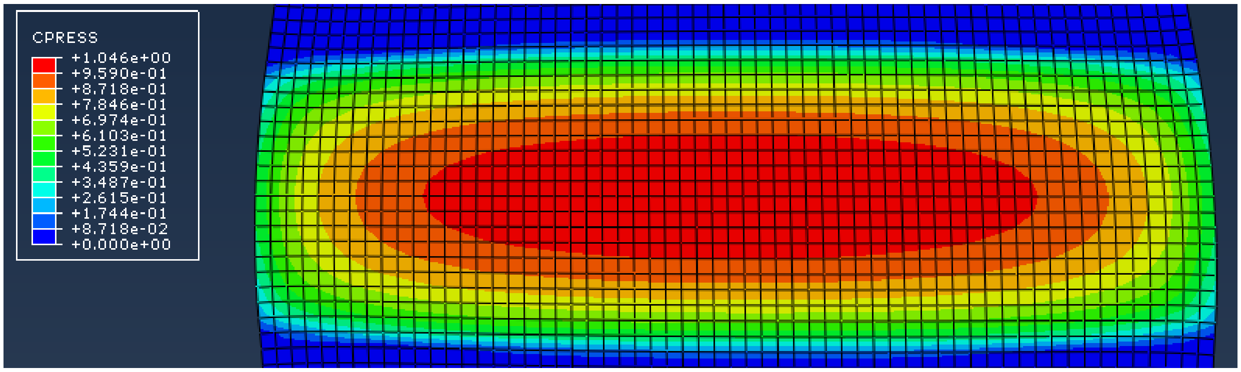

(b) F = 233 N

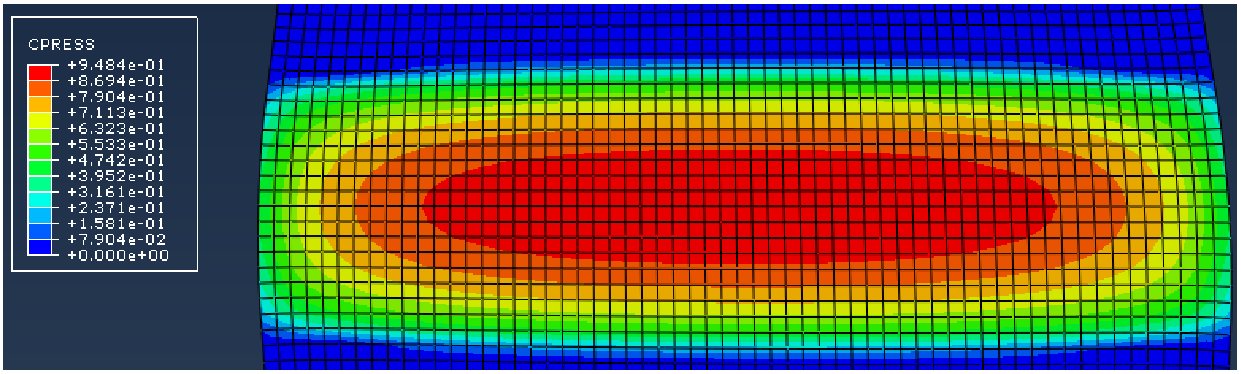

(c) F = 193 N

Figure 47. Compaction pressure distributions (MPa) in the baseline compaction roller at three different levels of process compaction force.

Ecoflex is used in the first generation of the smart roller to manufacture the sensor (also used as the compaction roller's tire). Young's modulus of the shore 00-30 durometer Ecoflex used, is estimated to be 0.1 MPa from the empirical trends observed in [33]. Even though the Young's modulus is quite low, the bulk behavior of rubbers is close to incompressible material behavior, making shear the primary mode of deformation for the roller's tire. A simple compression experiment (Figure 48) with a dummy roller is performed. A thicker tier (tier thickness = 12.5 mm) is used for the experiments to highlight roller deformation modes. It is interesting to note the that from 20 N to 220 N, this roller primarily shears out and gets separated from the hub rather than getting compressed radially over the nip point.

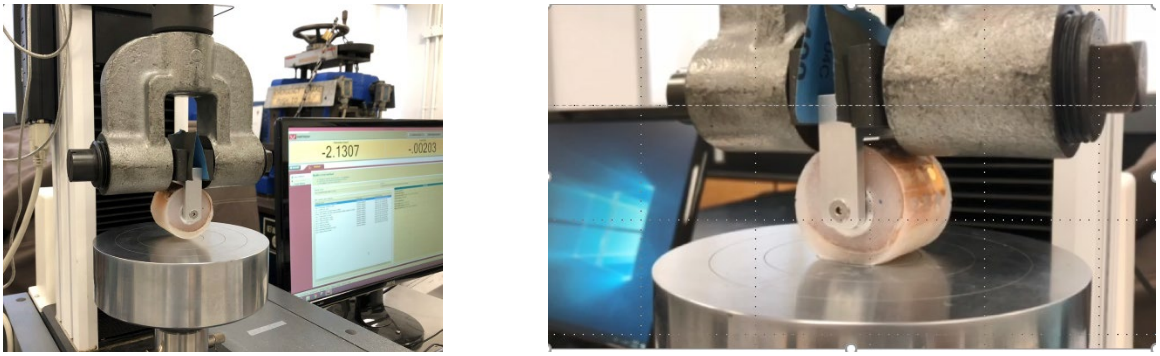

(a) Test setup **(b) F = 10 N**

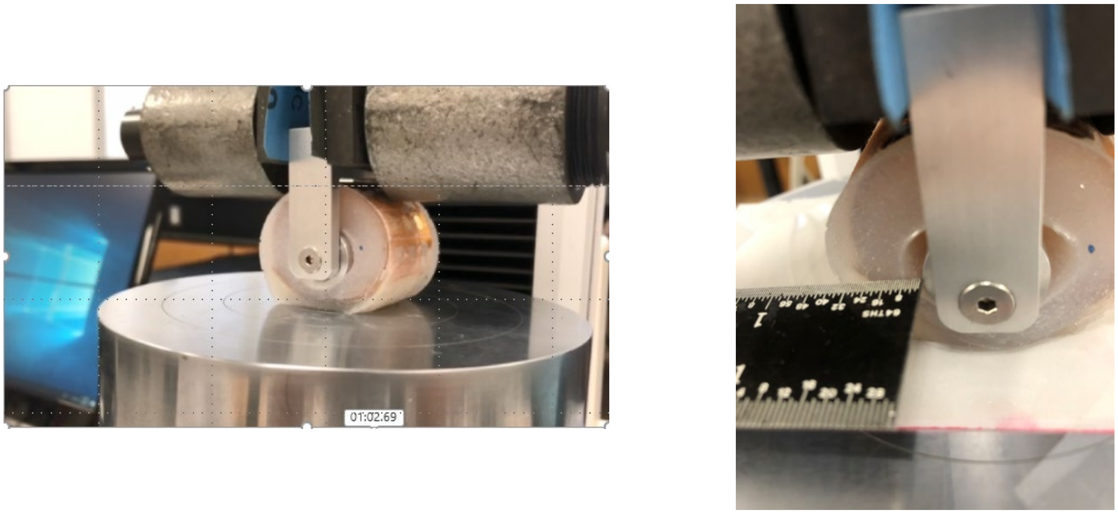

(b) F = 20 N **(b) F = 220 N**

Figure 48. Preliminary characterization of the roller tire material under compression.

It is important for the material model to properly represent roller behavior. A neo-Hookean material model combined with nonlinear geometry is used to represent roller behavior. For the neo-Hookean model to be consistent with the theory of elasticity at the small strain limit, the following relationships should exist between parameters of this model (C_1 and D_1) and shear and bulk moduli (G and K, respectively).

$$C_1 = G/2 \qquad (1)$$
$$D_1 = K/2$$

The external shell of the smart roller is 50 mm in diameter and a 3 mm-thick flexible tire (the sensor substrate) is adhered to the external shell (Figure 49). Although tire thickness in the smart roller is smaller than that in the baseline roller, the larger diameter of the relatively rigid part in the smart roller provides comparatively more stiffness for the overall roller structure.

Figure 50 (a) presents the compaction pressure distribution of the smart roller and compares it to the compaction pressure distribution of the baseline roller. The contact height for the smart roller is 16.8 mm and for the base line roller, it is 8.4 mm. Larger contact height is favorable in tack formation as it provides more time for the prepreg to be under pressure. At this compaction force, the peak value of pressure is 42% smaller for the smart roller. This could be compensated by increasing the compaction force, if required. Moreover, the smart roller produces a more uniform pressure distribution with a less sudden decrease of pressure, along the width (same as roller width) and height of contact area. More finite element simulations and experimental characterizations of rollers will allow for the roller dimensions (especially outer diameter of the external shell) and sensor thickness, to be further studied and optimized to develop a more coherent view of roller performance.

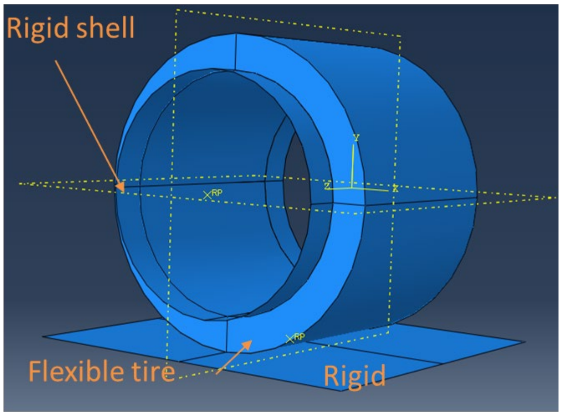

Figure 49. Geometry of the smart roller.

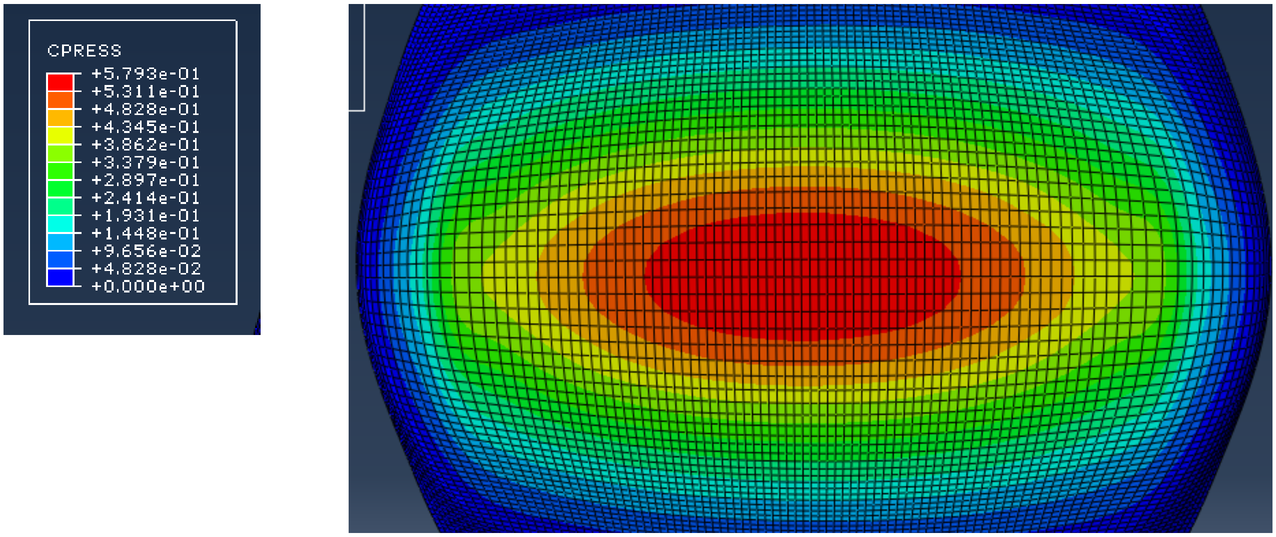

(a) Smart roller

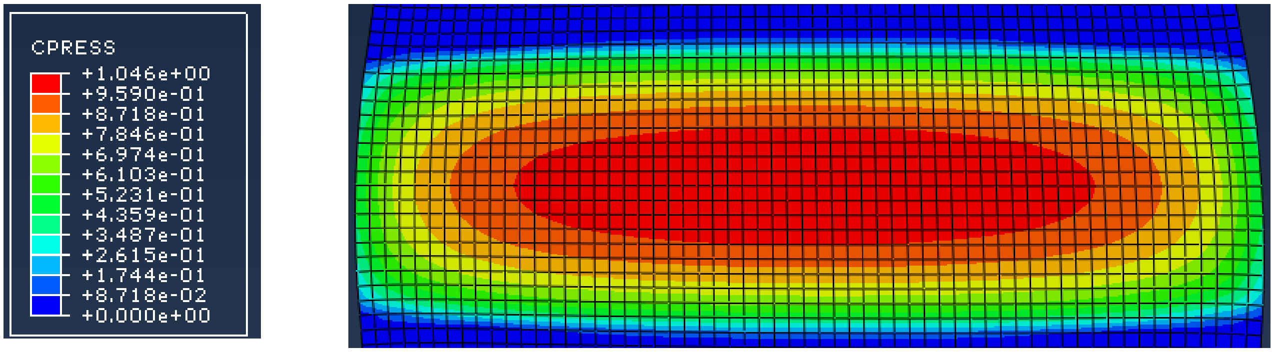

(a) Baseline roller

Figure 50. Compaction pressure (CPRESS) distributions of the rollers subjected to 240 N.

4.3 Think

4.3.1. High-fidelity Physics-based Models

A first generation of high-fidelity physics-based models simulate prepreg deposition and in-situ peel test performed by the physical AFP simulator. The deposition model (Figure 51) includes a thermal sub-model, a compaction sub-model and the tack cohesion model (developed previously under NASA ACP).

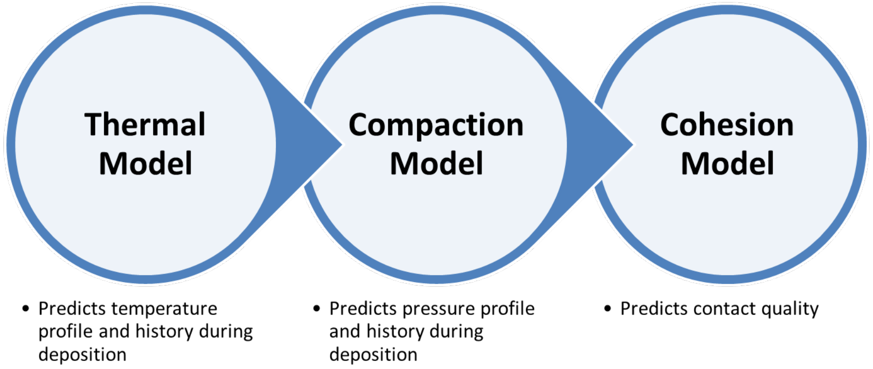

Figure 51. High-fidelity deposition model.

Interactions and dependencies of the modeling approach are presented in Figure 52. In this figure, blue color denotes material conditions (e.g. aging), green color denotes process parameters (e.g. temperature) and orange is an indication of intermediary model parameters.

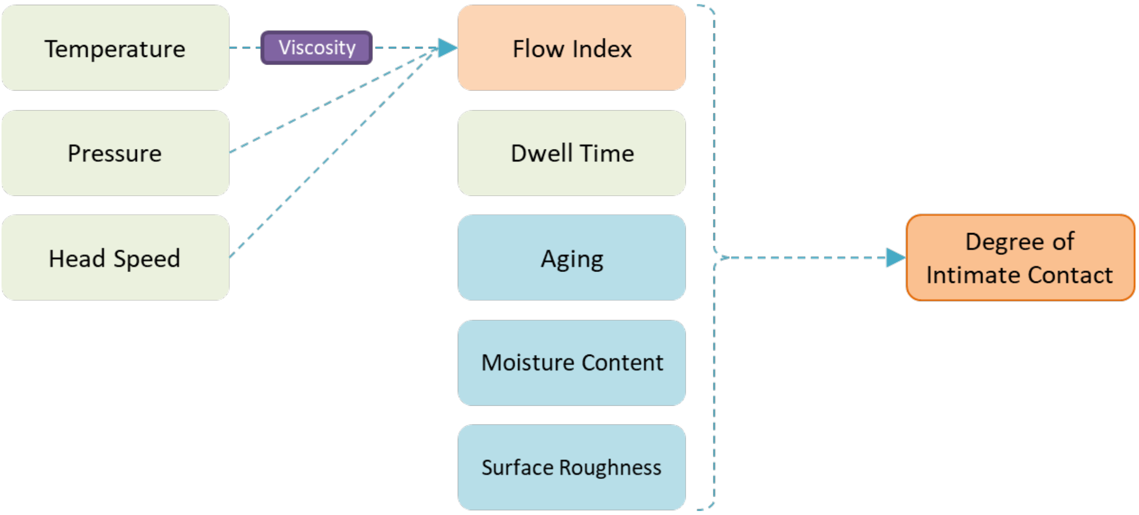

Figure 52. Cohesion sub-model of deposition.

Modulus and viscosity of the uncured prepreg is very sensitive to temperature variations. The thermal model simulates infrared emissions and radiation heat transfer during the process. It predicts temperature profiles and histories of the layup. The temperature profile is then fed into the compaction and cohesion models. Through-thickness prepreg stiffness that is needed in the compaction model is a function of resin and fiber bed moduli and therefore is affected by temperature. Moreover, viscosity directly affects flow index and degree of intimate contact, thus temperature profile is required to be known in the cohesion model.

The compaction model simulates dynamic roller behavior and prepreg response during deposition and predicts pressure profiles and histories. The pressure profile is provided as an input to the tack cohesion model (to determine flow index). In the cohesion model, Degree of Intimate Contact ($0 \leq DoIC \leq 1$) is predicted as a function of process and material parameters. When two prepregs are brought into contact, the true area of contact is very small (theoretically $DoIC = 0$). As temperature rises and compaction pressure is increased, resin bleeds into the inter-layer gaps, increasing the true area of contact which results in a more complete cohesion between the two prepreg layers. Ideally, complete contact is reached and $DoIC$ approaches the theoretical value of 1. $DoIC$ is used in the cohesion model as a state variable that defines the status of cohesion at the end of this stage.

The outcome of the peel test is peel resistance normalized by the tow width. This value is essentially equivalent to energy of separation characterized as the area below the traction-separation curve. This information is used to calibrate parameters of the tack model. Degree of intimate contact, calculated in the cohesion model, is provided as an input to the decohesion model. Viscoelastic behavior of the resin as well as mixed modalities are taken into account. Moreover, effects of temperature and rate are reduced using the principle of time-temperature superposition (Williams-Landel-Ferry equation) and are considered in the decohesion model (Figure 53).

More details of the physics-based modeling of tack were reviewed in section 2.4 and can also be found in the references cited therein.

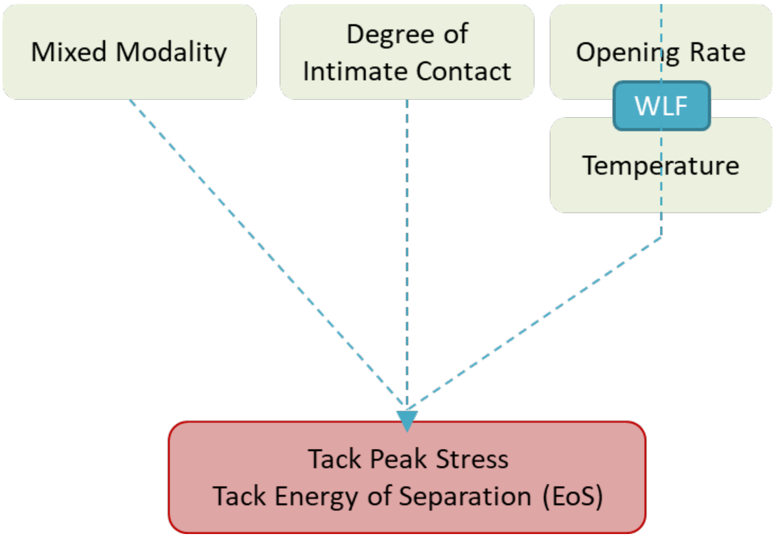

Figure 53. Decohesion model.

4.3.2. Real-time Virtual Twin

An important part of implementing the sense-think-act framework is to synthesize data gathered from the physical and virtual digital twins, and analyze them through the lens of our physics-based understanding of the AFP system in order to effectively control the processing parameters and define the process window.

The finite element method (FE) is a powerful tool for simulating the various complex physics and geometries involved in AFP. However, FE is typically not the best option for the active process control problem that is of interest in this work. Active control requires online updating of boundary conditions to determine system response to the imposed conditions. Commercial FE solvers are typically not compatible with boundary updating (a problem is solved for a given set of boundary conditions). On the other hand, complexity of the physics involved (e.g. nonlinear geometries and material parameters, contact, heat transfer, etc.) and the scale of the problem is such that, developing all of the physics from scratch in an open source FE solver is not practical.

One method of addressing this issue is using machine learning approaches to train surrogate models of the process. First it is required to produce large datasets over a wide range and combination of different process and material parameters. To do so, it is necessary to simplify the high-fidelity models described in 4.3.1. For example, instead of simulating the detailed temperature and pressure histories, the steady state uniform temperature as a function of substrate, infrared lamp power and deposition speed can be found. Moreover, mean compaction pressure could be found as a function of prepreg, roller material/geometry and compaction force.

After producing the large datasets, machine learning based models can be trained on the data. Real-time virtual tack model will be trained which allows us to predict process outcomes in a real time manner, and solve the inverse problem for optimal control of the process.

4.3.3. Integrated Modeling Approach

Traditionally, sensing and measurements are implemented in the process as inspections that are performed in addition to the main manufacturing process. In the automated fiber placement, layer-by-layer inspections and final part inspections are performed to ensure part quality. However, there is no method available that allows in-situ measurements of the process parameters to be linked to process quality outcomes.

In the conventional setting, many offline experiments are performed prior to the manufacturing process, to establish a link between microstructure and properties (Figure 54). Then, additional non-destructive inspections are performed after each step of the manufacturing to ensure desired microstructure is produced. There is not any real-time feedback directly from process to property that allows engineers to determine whether processing conditions used, are appropriate.

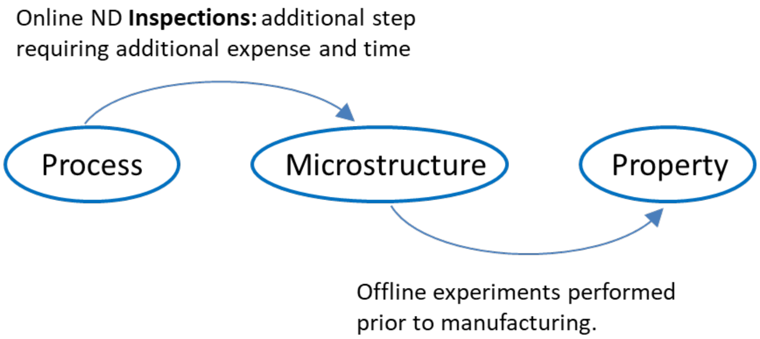

Figure 54. Process-microstructure-property relationship.

For the AFP system, different sensing technologies, such as image analysis, 2D and 3D profilometry, and Optical Coherence Tomography have been used as non-destructive methods of feature detection (i.e. defects such as puckers, overlaps/gaps, etc.). The data from these inspection technologies have been analyzed using conventional statistical approaches as well as machine learning approaches. These methods are all used as post-manufacturing inspections. The present work aims at developing an integrated framework that extends quality control to the processing stage achieves that by analyzing data measured during the manufacturing.

The Physical Digital Twin includes the table-top AFP system, and the standard sensors for process monitoring. Additionally, a smart, instrumented roller is under development that is able to provide local information about the interactions between prepreg, roller and substrate by measuring process parameters at the nip point of the AFP process. The Virtual Digital Twin includes the physics-based simulations and machine learning models described in sections 4.3.1 and 4.3.2. Uncertainty Quantification methodologies can be used to integrate the virtual models and physical data. UQ creates the feedback loop between the virtual and physical digital twins Figure 55.

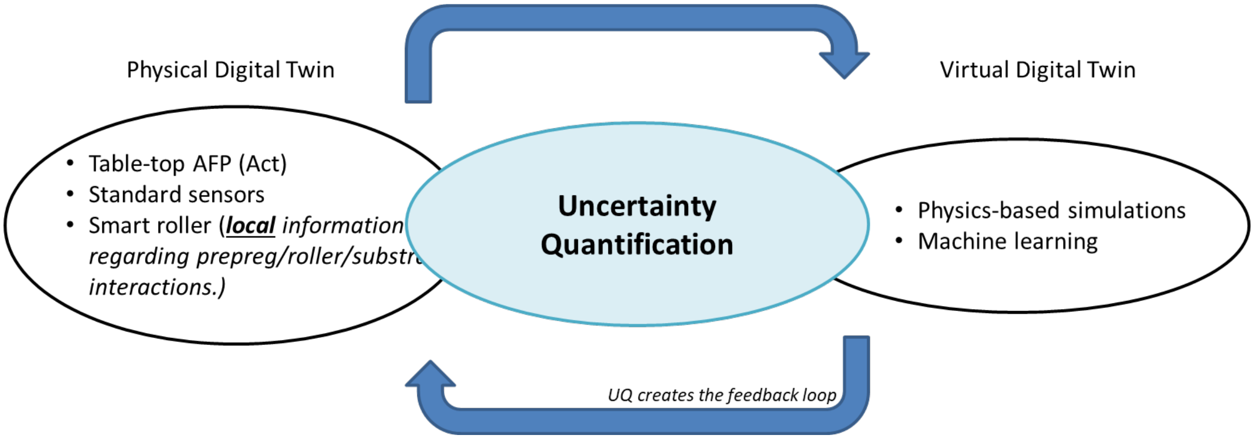

Figure 55. Integrated Analysis Framework.

Development of the integrated analysis framework allows for emergence of new information about the process, that could not have been accessed when studying each system individually. This new information essentially establishes a direct link between process to property (Figure 56). Finally, engineers will be able to deduce process quality outcomes from in-situ measurement of process conditions performed during the material processing. They will be able to determine quality of process conditions in real-time and determine the process window and control process conditions optimally.

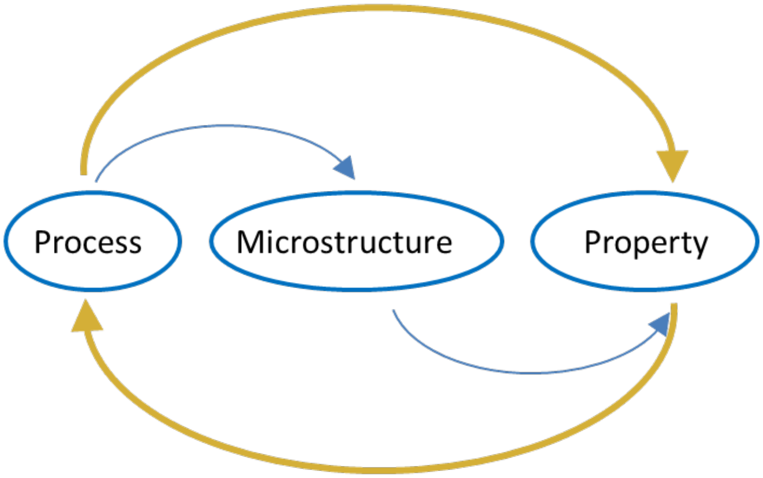

Figure 56. Process-microstructure-property relationship in the integrated framework.

5.0 CONCLUSIONS

Automated manufacturing is increasingly adopted by aerospace industry with the promise of higher production rates, higher reliability, and better quality. However, the success has been lower than expected thus far. For example, we are still unable to make complex parts using AFP in a fast and robust manner, and any change in material, geometry or process condition requires extensive testing.

In the past a few decades, considerable progress has been made in digital technologies, including automation, sensing, physics-based simulation, and the data sciences/uncertainty quantification. Individual technologies have been implemented in composites manufacturing to various degree in an ad hoc manner. The significance and innovation of the present work is to *integrate* these capabilities and customize them for composites manufacturing. In this manner, we can compensate for weaknesses in each individual digital technology and create significant value from the integration.

A small but representative, table-top AFP simulator is being built. The smaller scale and lower complexity of the system allows for an in-depth study of the system. The AFP cell can be thoroughly instrumented to measure all process parameters involved. Various design aspects of the AFP cell were discussed in this report. Standard sensor technologies used to monitor the process are presented. Development of a smart roller capable of measuring compaction pressure at the nip point of the process is reported and plans for further expansion of smart roller's capabilities are discussed.

Final steps of assembly of the AFP cell and its control system are being carried out. Once, assembly is finished, the setup will be used to experimentally characterize the smart roller. Moreover, the first set of AFP experiments will be performed (as summarized in Figure 57). The effect of varying speeds, compaction forces, and temperatures on tack will be investigated. The effect deposition rate and peel rate can be examined independently. Moreover, the effect of arbitrary substrate orientation on demonstrated tack levels will be studied.

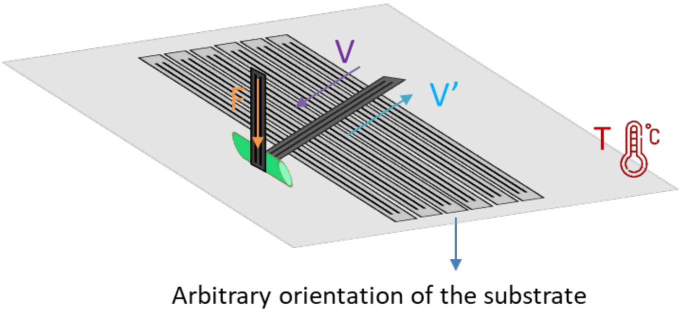

Figure 57. First set of AFP experiments.

6.0 REFERENCES

1. Composites Market Report: Trends, Forecast and Competitive Analysis. (2019).

2. Ashforth, C. and Ilcewicz, L. Comprehensive Composite Materials II. Elsevier: 2018.

3. ATL and AFP: Defining the megatrends in composite aerostructures. https://www.compositesworld.com/articles/atl-and-afp-defining-the-megatrends-in-composite-aerostructures

4. Evolving AFP for the next generation. https://www.compositesworld.com/articles/evolving-afp-for-the-next-generation

5. Russell, J., "Automation: The Next Big Thing for Aerospace Composites", https://www.linkedin.com/pulse/automation-next-big-thing-aerospace-composites-john-russell?trk=public_profile_article_view

6. ASTM D8336 - 21 - Standard Test Method for Characterizing Tack of Prepregs Using a Continuous Application-and-Peel Procedure.

7. Crossley, R. J. Characterisation of Tack for Automated Tape Laying. PhD Thesis, 07/2011.

8. Crossley, R. J., Schubel, P. J., and De Focatiis, D. S. A., "Time–temperature equivalence in the tack and dynamic stiffness of polymer prepreg and its application to automated composites manufacturing," *Composites Part A: Applied Science and Manufacturing*, **52**, September 2013, pp. 126–133.

9. Crossley, R. J., Schubel, P. J., and Warrior, N. A., "Experimental determination and control of prepreg tack for automated manufacture," *Plastics, Rubber and Composites*, **40**, 6–7, September 2011, pp. 363–368.

10. Crossley, R., Schubel, P., and Warrior, N., "The experimental determination of prepreg tack and dynamic stiffness," *Composites Part A: Applied Science and Manufacturing*, **43**, 3, 2012, pp. 423–434.

11. Endruweit, A., Choong, G. Y., Ghose, S., Johnson, B. A., Younkin, D. R., Warrior, N. A., and De Focatiis, D. S., "Characterisation of tack for uni-directional prepreg tape employing a continuous application-and-peel test method," *Composites Part A: Applied Science and Manufacturing*, **114**, 2018, pp. 295–306.

12. Budelmann, D., Detampel, H., Schmidt, C., and Meiners, D., "Interaction of process parameters and material properties with regard to prepreg tack in automated lay-up and draping processes," *Composites Part A: Applied Science and Manufacturing*, **117**, February 2019, pp. 308–316.

13. Wohl, C., Palmieri, F., Forghani, A., Hickmott, C., Bedayat, H., Coxon, B., Poursartip, A., and Grimsley, B., "Tack Measurements of Prepreg Tape at Variable Temperature and Humidity," *Proceedings of the Composites and Advanced Materials Expo, Orlando, FL*, 2017

14. Takahashi, K., Yamagata, Y., Inaba, K., Kishimoto, K., Tomioka, S., and Sugizaki, T., “Characterization of Tack Strength Based on Cavity-Growth Criterion,” *Langmuir: the ACS journal of surfaces and colloids*, **32**, 14, April 2016, pp. 3525–3531.

15. Forghani, A., Hickmott, C., Bedayat, H., Wohl, C., Grimsley, B., Coxon, B., and Poursartip, A., “A Physics-Based Modelling Framework for Simulation of Prepreg Tack in AFP,” *Proceedings of the Society for the Advancement of Material and Process Engineering – North America, Seattle, WA,* 2017

16. Forghani, A., Hickmott, C., Hutten, V., Bedayat, H., Wohl, C., Grimsley, B., Coxon, B., and Poursartip, A., “Experimental Calibration of a Numerical Model of Prepreg Tack for Predicting AFP Process Related Defects,” *Proceedings of the Society for the Advancement of Material and Process Engineering – North America, Long Beach, CA*, 2018

17. Forghani, A., Hickmott, C., Bedayat, H., Wohl, C., Grimsley, B., Coxon, B., and Poursartip, A., “Simulating Prepreg Tack in AFP Process,” *Proceedings of the American Society for Composites — Thirty-second Technical Conference*, **0**, 2017

18. Hutten, V., Forghani, A., Silva, P., Hickmott, C., Sreekantamurthy, T., Wohl, C., Grimsley, B., Coxon, B., and Poursartip, A., “A Validation Study of a Physics-based Tack Model for an Automated Fiber Placement Process Simulation,” *SAMPE 2019 - Charlotte, NC*, April 2019

19. Blueprint For Industry 4.0: What Manufacturers Must Do Today. https://www.forbes.com/sites/annashedletsky/2019/09/17/blueprint-for-industry-40-what-manufacturers-must-do-today-industrial-innovation-digital-factory/?sh=79cbd8595306

20. 21st Century Manufacturing Modeling and Simulation Research and Investment Needs. https://compositeskn.org/KPC/Reference:E6ceaa0b-9689-3f80-b3f4-0fa7ccdc9c32

21. Sinha, P., “The sense-think-act model,” *Siemens white paper*,

22. Calawa, R. and Nancarrow, J. Medium Wave Infrared Heater for High-Speed Fiber Placement. (2007).

23. Documentation of FESTO Toothed-belt axes ELGC-TB-KF. (2020).

24. Bakhshi, N. and Hojjati, M., “Effect of compaction roller on layup quality and defects formation in automated fiber placement,” *Journal of Reinforced Plastics and Composites*, **39**, 1–2, January 2020, pp. 3–20.

25. Lukaszewicz, D. H.-J. A., Ward, C., and Potter, K. D., “The engineering aspects of automated prepreg layup: History, present and future,” *Composites Part B: Engineering*, **43**, 3, April 2012, pp. 997–1009.

26. Sarwar, M. S., Dobashi, Y., Preston, C., Wyss, J. K. M., Mirabbasi, S., and Madden, J. D. W., “Bend, stretch, and touch: Locating a finger on an actively deformed transparent sensor array,” *Science Advances*, **3**, 3, March 2017, pp. e1602200.

27. Mischler, P.L., Tingley, M.C., and Hoffmann, K. Compaction roller for a fiber placement machine. (2010).

28. Johnson, B.A. Conformable compaction apparatus for use with a fiber placement machine. (2002).

29. Modeling and impact analysis on contact characteristic of the compaction roller for composite automated placement - Jinxiang Cheng, Dongbiao Zhao, Kai Liu, Yangwei Wang, Huaiyuan Chen, 2018. https://journals.sagepub.com/doi/10.1177/0731684418798151 (accessed Jun. 21, 2021).

30. Jiang, J., He, Y., and Ke, Y., "Pressure distribution for automated fiber placement and design optimization of compaction rollers," *Journal of Reinforced Plastics and Composites*, **38**, 18, September 2019, pp. 860–870.

31. Jiang, J., He, Y., Wang, H., and Ke, Y., "Modeling and experimental validation of compaction pressure distribution for automated fiber placement," *Composite Structures*, **256**, January 2021, pp. 113101.

32. Chu, Q., Li, Y., Xiao, J., Huan, D., and Zhang, X., "Placeability restricted by in-complete contact between laying roller and mould in an automated fiber placement process," *Journal of Reinforced Plastics and Composites*, **37**, 7, April 2018, pp. 475–489.

33. Mix, A. W. and Giacomin, A., "Standardized Polymer Durometry," *Journal of Testing and Evaluation*, **39**, 2011, pp. 696–705.

7.0 SYMBOLS, ABBREVIATIONS AND ACRONYMS

ACP	Advanced Composites Project
AFP	Automated Fiber Placement
DoIC	Degree of Intimate Contact
EoS	Energy of Separation
FI	Flow Index
IPC	Industrial PC (the central control device)
ML	Machine Learning
PCB	Printed Circuit Board
PDT	Physical Digital Twin
PFC	Phase-Fired Control
SCR	Silicon Controlled Rectifier
UQ	Uncertainty Quantification
VDT	Virtual Digital Twin